



## On-demand dual-stimuli-responsive hydrogels for localized and sustained delivery of MP-L [I5R8] to treat bacterial wound infections

Marcelo Guerrero <sup>a,1</sup>, Adolfo Marican <sup>b</sup>, Diana Rafael <sup>c,d,e</sup>, Fernanda Andrade <sup>c,d,f</sup>, Rodrigo Moore-Carrasco <sup>g</sup>, Sekar Vijayakumar <sup>h</sup>, Paulo Salinas <sup>i</sup>, Gustavo Cabrera-Barjas <sup>j</sup>, Juan Lara <sup>k</sup>, Esteban F. Durán-Lara <sup>a,\*</sup>

<sup>a</sup> Laboratory of Bio & Nano Materials, Drug Delivery and Controlled Release, Department of Microbiology, Faculty of Health Sciences, University of Talca, Talca 3460000, Chile

<sup>b</sup> Institute of Chemistry of Natural Research, University of Talca, Talca 3460000, Chile

<sup>c</sup> ClinicalBiochemistry, Drug Delivery and Therapy Group (CB-DDT), Vall d'Hebron Institutof Research (VHIR), Vall d'Hebron University Hospital, Vall d'Hebron BarcelonaHospital Campus, Passeig de la Vall d'Hebron, 119-129, Barcelona 08035, Spain

<sup>d</sup> Centro de Investigación Biomédica en Red de Bioingeniería, Biomateriales y Nanomedicina (CIBER-BBN), Instituto De Salud Carlos III, Madrid, Spain

<sup>e</sup> Functional Validation & Preclinical Research (FVPR)/U20 ICTS Nanobiosis, Vall d'Hebron Institut de Recerca (VHIR), Barcelona 08035, Spain

<sup>f</sup> Department of Pharmacy and Pharmaceutical Technology and Physicochemistry, Faculty of Pharmacy and Food Sciences, School of Pharmacy, Universitat de Barcelona (UB), Av. de Joan XXIII, 27-31, Barcelona 08028, Spain

<sup>g</sup> Departamento de Bioquímica Clínica e Inmunohematología, Facultad de Ciencias de la Salud, Universidad de Talca, P.O. Box 747, Talca 3460000, Chile

<sup>h</sup> College of Material Science and Engineering, Huaqiao University, Xiamen 361021, PR China

<sup>i</sup> Laboratory of Animal & Experimental Morphology, Institute of Biology, Faculty of Sciences, Pontificia Universidad Católica de Valparaíso, Valparaíso, Chile

<sup>j</sup> Facultad de Ciencias del Cuidado de la Salud, Universidad San Sebastián Campus Las Tres Pascualas, Lientur 1457, Concepción 4080871, Chile

<sup>k</sup> Chile Laboratory Animal Research Facility, Research Direction, University of Talca, Av. Lircay s/n, Talca 3460000, Chile

<sup>1</sup> PhD Program in Science, R&D Bioactive Products Department, Chemistry Institute of Natural Resources, University of Talca, Talca, Chile

### ARTICLE INFO

#### Keywords:

Stimuli-responsive hydrogel  
Sustained release  
Drug delivery  
Antimicrobial peptide  
Multi-drug resistant bacteria

### ABSTRACT

This study presents the development of two novel injectable dual-responsive polyanionic hydrogels (DRPHs) based on N-isopropylacrylamide (NIPAM), incorporating carboxylic acid comonomers for temperature- and pH-responsive drug release. These hydrogels were designed for the sustained and localized delivery of the antimicrobial peptide MP-L [I5R8], targeting multidrug-resistant bacteria (MDRB) in wound infections. The physicochemical characterization confirmed polymer formation and comonomer integration through Fourier-transform infrared spectroscopy (FTIR) and nuclear magnetic resonance (NMR). Rheological analysis demonstrated a temperature-dependent sol-gel transition at  $\sim 35^\circ\text{C}$ , making the hydrogels suitable for *in situ* gelation at physiological conditions. The hydrogels exhibited tunable swelling behavior and a controlled dual-phase release profile of MP-L [I5R8], ensuring both immediate bactericidal activity and prolonged antimicrobial effect. *In vitro* assays confirmed sustained antimicrobial efficacy against *Staphylococcus aureus* and *Pseudomonas aeruginosa*, while biocompatibility tests validated their safety for biomedical applications. An *in vivo* diabetic wound infection model demonstrated rapid infection clearance, enhanced wound healing, and organized tissue regeneration following treatment with MP-L [I5R8]-loaded DRPHs. These results highlight the potential of dual-stimuli-responsive hydrogels as a next-generation antimicrobial delivery platform for the treatment of chronic infected wounds, such as diabetic foot ulcers.

### 1. Introduction

Multidrug-resistant bacteria (MDRB) have become a major global health problem [1]. The World Health Organization (WHO) has declared an international alert, estimating that deaths caused by

MDRB-associated infections will exceed those caused by cancer by 2050 [2,3]. Surgical wound infections, particularly diabetic foot ulcer infections (DFUIs), are among the most challenging to treat [4,5]. The bacterial species most frequently isolated in these infections are *Staphylococcus aureus*, and *Pseudomonas aeruginosa*. Moreover, *P. aeruginosa*

\* Corresponding author.

E-mail address: [eduran@utalca.cl](mailto:eduran@utalca.cl) (E.F. Durán-Lara).

has a high intrinsic resistance to various antibiotics, making their isolation alone a challenging and expensive treatment [6,7]. On the other hand, *S. aureus* is the predominant bacterium in DFUI, including methicillin-resistant species (MRSA) [8].

Antimicrobial peptides (AMPs) are a promising alternative to conventional antibiotics for treating and preventing infections caused by MDRB [9,10]. These peptides, derived from natural sources like plant secondary metabolism or insect venom, have shown efficacy against pathogenic microorganisms [11,12]. AMPs are short sequences of fewer than 100 amino acids, containing positively charged residues such as lysine, arginine, and histidine, with a net charge of +2 to +9 and about 50 % hydrophobic residues [13,14]. Their cationic nature allows them to form amphipathic structures by interacting with bacterial membranes [15,16]. Their effectiveness partly stems from their ability to adopt specific secondary structures under various environmental conditions [17]. While the effectiveness of  $\beta$ -sheet structures is debated,  $\alpha$ -helix structures are generally more effective against bacteria [18]. Numerous  $\alpha$ -AMPs with antibacterial activity are documented, and several databases compile these peptides. It is also possible to modify derivatives to enhance their qualities for specific research needs [19]. One example is mastoparan, a 14-residue peptide toxin derived from wasp venom, which has demonstrated significant medical potential against antibiotic-resistant clinical isolates. Mastoparan induces mast cell degranulation and histamine release. In 2016, Irazazabal et al. modified the original mastoparan peptide by substituting alanine with isoleucine at position 5 and alanine with arginine at position 8, creating MP-L [I5R8]. This modification increased the peptide's net positive charge and conferred broad-spectrum antimicrobial activity against bacteria without inducing hemolysis or cytotoxicity in HEK-293 cells. Additionally, MP-L[I5R8] is effective against *S. aureus* and *P. aeruginosa* [20]. MP-L[I5R8] exhibits essential characteristics that make it a promising candidate for treating bacterial infections. It has a short, linear sequence of 14 amino acids, a net positive charge of +4, and an  $\alpha$ -helix secondary structure in solution. Other authors have reported this structural feature as a key determinant of the antibacterial activity of peptides [21,22]. A relevant aspect is the  $\alpha$ -helix structure of the peptide in solution, which has been corroborated by bioinformatics studies previously conducted by our group. In these studies, its effectiveness was also compared with that of  $\beta$ -folded peptides [23]. Furthermore, a review of the literature and the DRAMP (Data Repository of Antimicrobial Peptides) database conducted by our group confirms that more than 80 % of antimicrobial peptides reported to date as antibacterial adopt an  $\alpha$ -helix secondary structure. Additionally, peptides with the highest antibacterial efficacy typically have a linear sequence of no more than 50 amino acids. MP-L [I5R8] meets all these characteristics, unlike many AMPs reported in the literature [24].

Despite their advantages, the clinical application of AMPs as new peptide antibiotics faces challenges such as short half-life, instability, susceptibility to enzymatic degradation, and potential toxicity to human cells [19,20]. In this context, combining AMPs with drug delivery systems (DDS) like stimulus-responsive hydrogels offers a promising alternative due to their high biocompatibility, adjustable release rates, and versatility for loading different molecules. Each AMP presents unique characteristics such as structure, spatial conformation, charge, and amphipathic nature [25]. Therefore, designing hydrogels that consider the interaction affinity with AMPs is essential to achieve high-release performance and protect the antimicrobial properties of the peptide.

Hydrogels (HGs) are three-dimensional (3D) networks of hydrophilic polymers capable of absorbing large amounts of water or biological fluids [26]. These networks are formed by cross-linked monomers or polymer chains through covalent and non-covalent interactions such as hydrogen bonds and electrostatic interactions [27]. The HGs can be classified by cross-linking type, size, sensitivity to stimuli, ionic charge, degradability, polymer origin, and synthesis methods [27,28]. Stimuli-responsive HGs, particularly those sensitive to pH and

temperature changes, are extensively studied for their potential in biomedical applications [28]. Thermoresponsive HGs exhibit reverse thermal gelation (RTG), where increased hydrophobic interactions at higher temperatures form 3D network junctions [29]. pH sensitivity involves functional groups within the polymer chain that respond to environmental pH changes, resulting in a net hydrogel (HG) charge and enabling interactions with charged drugs [29,30]. Various stimuli-responsive HGs, including poly (N-isopropyl acrylamide) (pNIPAM) HGs, have been developed. pNIPAM has a lower critical solution temperature (LCST) of 32–34 °C, making it suitable for injectable drug carriers [31]. Loading hydrophilic peptide compounds into these HGs at low temperatures reduces the risk of denaturation [32]. Once injected, the solution becomes a temperature-activated HG, which acts as a sustained-release drug reservoir for localized delivery, useful for treating wounds such as diabetic foot ulcers (DFUI), which are characterized by irregular chronic wounds that go deeper into the tissue, even capable of reaching and infecting bone tissue [33]. Drug release from these HGs occurs first by diffusion, then by a combination of diffusion and degradation maintaining a sustained release [34]. On the other hand, the phase change property responding to temperature would allow filling and adapting the treatment to the depth and structure of the infected wound, unlike treatment with dressings [35,36].

Each AMP has a unique amino acid sequence, which requires tailoring the HG structure to a specific AMP by introducing different comonomers and cross-linkers to the NIPAM monomer. Multiple functional groups in the HG matrix can be pH-sensitive, interacting strongly with the cationic groups of AMPs [37,38]. The development of polyanionic HGs containing carboxylic acids in their structure increases the negative charge of the network at physiological pH, allowing interactions with positively charged amino acids in AMPs (e.g., lysine and arginine). These interactions can delay AMP release, allowing controlled drug release while preserving bioactivity [39,40].

This study proposes the development of two injectable, dual-responsive polyanionic HGs (DRPH) based on NIPAM with pH-sensitive carboxylic acid comonomers. This design enables electrostatic interactions with positively charged drugs such as AMP MP-L [I5R8], providing sustained and localized antimicrobial release. Physicochemical characterization of DRPHs such as Fourier transform infrared spectroscopy (FTIR), scanning electron microscopy (SEM), nuclear magnetic resonance (NMR), swelling behavior, mechanical strength, thermal stability, and MP-L[I5R8] release kinetics have been carried out. Furthermore, the biocompatibility and antimicrobial efficacy of MP-L [I5R8]-loaded DRPHs against *S. aureus* and *P. aeruginosa* were evaluated *in vitro* and *in vivo* to assess their potential as advanced drug delivery systems for wound treatments, such as DFUIs. This approach offers a promising way to address the limitations of traditional therapies.

## 2. Materials and method

### 2.1. Materials

N-isopropylacrylamide (NIPAM, 99 %), Trans- $\beta$ -Hydromuconic acid (Hy, 98 %), Maleic acid (Ma, 99 %), Poly(ethylene glycol) diacrylate (PEGDA,  $M_n = 700$ ), N,N'-Methylenbis(acrylamide) (MBA, 99 %), ammonium persulfate (APS, 98 %) N,N,N',N'-tetramethylenediamine (TEMED, 99 %) and trifluoroacetic acid (TFA, p.a. 98–100 %) were purchased from Merck (Darmstadt, Germany). Acetonitrile (ACN, HPLC grade) was purchased at PanReac AppliChem (Darmstadt, Germany). Ultra-pure water was obtained from a Heal Force NW Ultra-pure Water System. Antimicrobial peptide MP-L [I5R8] sequence INLKILARLAKKIL was synthesized by Shanghai RoyoBiotech Co., Ltd. Bacterial strains ATCC 25923 *Staphylococcus aureus*, and ATCC 27853 *Pseudomonas aeruginosa*, was commercially purchased from American type culture collection (ATCC). Mueller-Hinton agar culture medium, Mueller-Hinton broth was purchased at MERCK, Chile. Dimethyl sulfoxide

(DMSO), and 3-(4,5-dimethylthiazol-2-yl)-2,5-diphenyltetrazolium bromide (MTT) were provided by Merck (Spain). Presto Blue® cell viability reagent was provided by ThermoFisher Scientific (Spain). NIH-3T3 (ATCC® CRL-1658™) fibroblast cell line was purchased from the American Type Culture Collection (ATCC, LGC Standards, Spain). DMEM cell culture media, fetal bovine serum (FBS), penicillin-streptomycin mixture, phosphate-buffered saline (PBS) pH 7.4, and trypsin- Ethylenediaminetetraacetic acid (EDTA) and penicillin-streptomycin mixture were purchased from ThermoFisher Scientific (Spain). L-glutamine was obtained from Lonza (Spain). Transwell® permeable supports (Corning®) with permeable polyester membrane were purchased from Merck (Spain). Topical ointments of 1 g mupirocin (2 %) and 1 g silver sulfadiazine (1 %) were purchased from Pharmacy® Checker. For the *in vivo* model, Sprague Dawley (SD) rats were obtained from the University of Chile. The care, monitoring, and protocol were carried out at the University of Talca under protocol n°2023-01 associated with project 1210476, approved on May 11, 2023, by Comité Institucional de Ética, Cuidado y Uso de Animales de Laboratorio (CIEC-UAL). Streptozotocin (STZ ≥98 % purity, molecular weight 265.2 g/mol) was purchased from Santa Cruz Biotechnology.

## 2.2. DRPH synthesis

The synthesis of DRPHs was carried out by free radical polymerization. Briefly, different proportions of the constituents of both formulations; pNiHyPH: NIPAM (M1), Hy (M2), PEGDA (CL1), and pNiMaMH: NIPAM (M1), Ma (M3), MBA (CL2), Table 1, were added to form a homogeneous solution dissolved in 1 mL of ultrapure water, and 64 µL of TEMED solution was added. The reaction mixtures were kept under constant stirring for 15 min with nitrogen gas ( $N_2$ ) application. Later, 22 µL of APS (10 % w/w in ultrapure water) was added to start the reaction under constant stirring for 4 h. Subsequently, the HGs were stored at 4 °C for 30 min. Gelation capacity was verified at temperature ranges of 30–45°C. Those HGs with gelation temperatures within the mentioned range were washed in cellulose membrane (Cut-off 14.000 Da) for 48 h with water change every 8 h. Finally, the HGs were lyophilized for 48 h in a freeze dryer (BK-FD12PT) after freezing overnight at –20°C. Once the purified DRPHs were obtained, the physical-chemical characterization was carried out, as the determination of the MP-L [I5R8] release profile, biocompatibility assays, and *in vitro* and *in vivo* antibacterial activity.

## 2.3. DRPHs characterization

### 2.3.1. Fourier transform infrared spectroscopy (FTIR)

The freeze-dried DRPHs were analyzed utilizing a single-reflection ATR measuring attachment (QATR-S), facilitating direct assessment of the solid samples. This was performed using an IRSpirit FTIR Shimadzu throughout a spectrum of 4000–500 cm<sup>-1</sup> at a resolution of 4 cm<sup>-1</sup>, employing 32 scans on ATR.

### 2.3.2. Nuclear magnetic resonance (<sup>1</sup>H NMR)

The <sup>1</sup>H NMR analyses have been carried out in the nuclear magnetic resonance (NMR) using the AVANCE™ III 400 MHz NMR spectrometer (Bruker Corporation, USA). Spectra were recorded in Deuterium oxide ( $D_2O$ ).

**Table 1**

Molar proportions of each building block used for the synthesis of DRPHs.

	% Molar M1	% Molar M2	%Molar CM3	%Molar CL1	%Molar CL2
pNiHyPH	68,5	27,4	-	4,1	-
pNiMaMH	70,4	-	28,2	-	1,4

(\*) The proportions of each building block in the hydrogels were determined based on their sol-gel transition capacity and temperature response at > 33°C

### 2.3.3. Thermogravimetric analysis (TGA)

The thermal stability of pNiHyPH and pNiMaMH were analyzed with a SNETZSCH TG 209F3 instrument. Approximately 3 mg of freeze-dried sample was placed into the instrument balance and heated at a constant heating rate of 10 °C min<sup>-1</sup>. The heating was conducted from 25 °C to 600 °C in  $N_2$  or air as a reactive gas (with a mass flow of 50 mL min<sup>-1</sup>). The temperature was held at 600 °C for 30 min to allow the oxidation process to complete. The first region of the thermal analysis, from room temperature to 600 °C under an  $N_2$  atmosphere, examines the thermolabile molecules or fragments that can be decomposed by simply heating the samples, such as the functional groups. The second region, the oxidative process (under O<sub>2</sub>), aims to observe the sample's oxidative resistance under extreme conditions, reactive gas (dynamic air atmosphere), and high temperature (600 °C) [41].

### 2.3.4. Rheological analysis

The physical characterization of the DRPHs was conducted using an MCR702e Multidrive Rheometer/Dynamic Mechanical Analyzer (Anton Paar, Austria), coupled with a Peltier temperature control device (model P-PTD 220). A measuring parallel plate with a 50 mm diameter (model PP50) was used. The conditions for gelation measurement, including the determination of storage modulus (G'), loss modulus (G''), and loss factor (tan δ), were as follows: 128 points (0.2 min), shear deformation (γ) of 0.5 %, frequency (f) of 1 Hz, and a temperature range from 25 to 45 °C, applying a normal force of 0 N.

### 2.3.5. Scanning electron microscopy (SEM)

SEM was performed at the Nanostructured Liquid Characterization Unit of NANBIOSIS ICTS (Unit 12) (IQAC-CSIC, Barcelona, Spain). Briefly, samples were lyophilized using a VirTis BenchTop freeze dryer (SP Scientific) for 24 h, with a drying temperature of 0 °C for both samples. DRPHs, previously prepared and washed by dialysis, were placed in independent vials and brought to 25 °C and 35 °C in a thermoregulated bath to ensure the sol-gel transition. They were then immediately treated with liquid nitrogen for rapid freezing, preserving their structure for subsequent microscopic analysis. Lyophilized samples at different temperatures (25 °C and 35 °C) were mounted on aluminum stubs with carbon adhesive to secure them properly. Imaging was performed using the SEM TM-4000 Plus II (Hitachi) configured with an accelerating voltage of 15 kV for a balance between surface detail and depth of penetration. The working distance was maintained at 10 mm for optimal resolution and focus. Initial scans were conducted at a magnification of × 100 to locate the areas of interest, and detailed imaging was carried out at magnifications ranging from × 100 to × 1000. The chamber pressure was kept low to prevent sample charging. Images were captured and analyzed using the integrated Hitachi Map 3D software.

### 2.3.6. Gelation time and phase transition studies

Gelation time was measured using the CoatronX coagulometer. Each DRPH was reconstituted at 10 % w/v in pH 7,4 buffer solution. For quantification, 70 µL of the liquid DRPH was dispensed into a previously tempered cuvette inside the equipment (35 °C). The measurement begins when the DRPH is injected, and the time is determined through turbidimetric measurement. Phase transition studies were performed for both formulations to assess the effect of temperature. Optical transmittance changes of pNiHyPH (10 % w/v) and pNiMaMH (10 % w/v) were measured at 600 nm wavelength by utilizing a UV-vis spectrophotometer (UV-1800, Shimadzu, Japan) with a heating rate of 1 °C/min, in a range of 20–45°C.

### 2.3.7. Swelling degree determination

A certain amount of phosphate-buffered saline (PBS) (pH 7.4) was added to 1.5 mL Eppendorf tubes containing a known mass of dry DRPHs. These tubes were then heated to 35 °C and left to soak up the PBS. After predetermined time intervals, each sample was removed, and

any unabsorbed water was carefully removed. The swollen hydrogel sample (HS) was then promptly weighed. The equilibrium swelling ratio (%ESR) of the DRPHs was estimated according to the following equation [42]:

$$\%ESR = \frac{W_w - W_d}{W_d} \times 100 \quad (1)$$

where  $W_w$  is the weight of the swollen sample after carefully removing surface moisture with absorbent paper, and  $W_d$  is the weight of the dry sample recorded after freeze-drying.

#### 2.4. AMP loading, release kinetics profile and mathematical models

AMP loading into DRPHs was performed by mixing 1000 µL of MP-L [I5R8] from a 10 mg/mL (10,000 ppm) standard solution with 1000 µL of pNiHyPH or pNiMaMH, each reconstituted in PBS at 20 % w/v. Each MP-L[I5R8]-loaded DRPH was kept under constant stirring for 24 h at room temperature, resulting in a final MP-L[I5R8] concentration of 5 mg/mL (5000 ppm) within each hydrogel and a final DRPH concentration of 10 % w/v. Each MP-L [I5R8]-loaded DRPH was kept under constant stirring for 24 h at room temperature. 1000 µL of MP-L [I5R8]-loaded pNiHyPH and MP-L [I5R8]-loaded pNiMaMH were placed into the dialysis tubing (cellulose membrane, cut-off = 14,000 Da) and 4 mL of PBS pH 7,4 was used as release media. The samples were incubated at 35.0 ± 0.1 °C and shaken at 35 ± 2 rpm [43]. At different time points, 1000 µL of release medium was collected and replaced with an equal volume of PBS to maintain sink conditions throughout the study. The release rate of MP-L [I5R8]-loaded DRPHs were acquired by applying the concentration of released peptide to the following correlation, where CRPep is the cumulative release of MP-L [I5R8], CAPep is the cumulative amount of MP-L [I5R8] released and IAPep, the initial amount of MP-L [I5R8] presented in eq 2 [44]:

$$CRPep(\%) = \frac{CAPep}{IAPep} \times 100 \quad (2)$$

High-Performance Liquid Chromatography (HPLC) determined the released concentration of MP-L [I5R8]. The chromatographic system consisted of a Young in Chromass HPLC-PDA (Young in Chromass Co. Ltd., Gyeonggi-do, South Korea), model YL9100 Plus +, with PDA detector, and a C-18 100-RP-18(e) (250 mm × 4.0 mm i.d. × 4 µm) (MZ-Analysentechnik GmbH, Germany). The software used for signal integration was YL-Clarity. One hundred microliters of the sample were injected into the HPLC apparatus. Table S1 summarizes the Gradient elution with acetonitrile (TFA 0.01 %)/water (TFA 0.01 %). The flow rate was constant at 1 mL min⁻¹. The analytical wavelength was 220 and 280 nm at room temperature.

#### 2.5. Biocompatibility of pNiHyPH, pNiMaMH and MP-L [I5R8]

##### 2.5.1. Hemolytic assay on RBC

The hemolytic activity of the MP-L [I5R8] on red blood cells from healthy donors was evaluated following the protocol of Sæbø I, et al. [45]. Briefly: Blood samples obtained with heparin as an anticoagulant were centrifuged at 1700 g for 5 min. The red blood cells obtained were washed 3 times with PBS and a 1 % dilution of RBC was prepared. 100 µL of RBC was mixed with 100 µL of the different MP-L [I5R8] concentrations and incubated for one hour at 37 °C. The samples were centrifuged, and hemolysis was measured in 96-well plates at 540 nm. PBS pH 7.4 was used as a negative control for hemolysis. In contrast, Triton-X at 10 % was used as a positive control. The assay was performed in triplicate and the results are presented as % hemolysis compared to the positive control ± SD.

##### 2.5.2. Fibroblast cytotoxicity

Cell line and culture conditions. NIH-3T3 cells were grown in DMEM with 15 % FBS, a 1 % penicillin-streptomycin mixture, 2 mM L-

glutamine, and 1 % NEAA. The cells were maintained at 37 °C in a 5 % CO<sub>2</sub>-saturated atmosphere and were harvested from culture plates with 0.25 % trypsin-EDTA.

Cytotoxicity and biocompatibility evaluation of free MP-L [I5R8]. The biocompatibility of the free MP-L [I5R8] in fibroblasts was performed through the MTT assay in adhesion conditions. Briefly, 5000 cells were seeded in 96-well plates and incubated overnight to promote cell adhesion. Then cells were treated with serial dilutions of the free peptide and incubated for 72 h. Complete medium and 10 % DMSO were used as a negative and positive control of toxicity, respectively. Cell viability was measured using the MTT reagent according to the manufacturer's instructions. The formed formazan crystals in each well were solubilized with 100 µL of DMSO and the resultant absorbance was read at 590 and 630 nm (for background subtraction) with a microplate reader (Varioskan LUX, ThermoFisher Scientific, Spain). Prism 8 software (GraphPad Software, Inc.) calculated the half-maximal inhibitory concentration (IC50) by nonlinear regression of the concentration-effect curve.

Cytotoxicity and biocompatibility evaluation of hydrogel-based formulations. The biocompatibility of pNiHyPH and pNiMaMH was performed through a semi-direct contact test using permeable supports (Transwell® inserts). This technique has been widely adopted to evaluate the cytotoxicity of medical products such as HGs and other scaffolds, with comparable results to those obtained from conventional assays [46–48]. Briefly, 50,000 cells were seeded in 24-well plates and allowed to grow for 24 h and form a cell monolayer. Then 200 µL of each DRPH formulation was placed in the apical side of the inserts and incubated for 48 h. After the incubation period, the inserts were removed, and the Presto Blue® viability reagent was used to measure cells' metabolic activity, according to the manufacturer's instructions and using complete medium and 10 % DMSO as negative control and positive toxicity control, respectively. The absorbance was read at 570 in a microplate reader.

#### 2.6. In vitro antibacterial activity of biocompatibility of MP-L [I5R8]-loaded DRPHs

*In vitro*, antibacterial activity assays were performed following the recommendations of the Clinical Laboratory Standards Institute (CLSI) M-100 document [49]. Inherent antibacterial activity of the empty DRPHs and MP-L [I5R8]-loaded DRPHs was evaluated using the Kirby-Bauer diffusion assay on Mueller-Hinton agar plates for screening antibacterial activity against bacterial strains of *S. aureus* ATCC 25923, and *P. aeruginosa* ATCC 27853. Briefly, from overnight bacterial cultures, standardized 0.5 McFarland concentration solutions were prepared by spectrophotometric measurement 0.08–0.1 A.U. at 625 nm 1 × 10<sup>8</sup> CFU/mL, which were seeded on MH agar. 6 mm diameter wells were made and 80 µL of empty DRPHs and MP-L [I5R8]-loaded DRPHs were dispensed. The plates were incubated for 18 h at 37 °C for later reading. Furthermore, this technique was used to evaluate the prolonged antibacterial activity of the aliquots obtained from the cumulative peptide release assay. The minimum inhibitory concentration (MIC) of the MP-L [I5R8] was determined in 96-well plates. A 1 × 10<sup>5</sup> dilution of each bacterium in MH broth was obtained. 100 µL of this preparation was dispensed into the wells, always leaving position 11 as a positive growth control and the last column (position 12) free of bacteria as a negative growth control (200 µL of MH broth). The different dilutions of the MP-L [I5R8] were dispensed in equal amounts. The plates were cultured for 18 h at 37 °C for later reading in a microplate reader at 600 nm. Furthermore, this technique was used to evaluate the prolonged antibacterial activity of the aliquots obtained from the cumulative peptide release assay. Additionally, the minimum bactericidal concentration (MBC) and a time-kill assay were performed following previously reported protocols for their determination [20,50,51]. Each assay was performed in triplicate.

## 2.7. In vivo antibacterial activity of biocompatibility of MP-L [I5R8]-loaded DRPHs

The study was conducted on adult male SD rats (200–350 g) acquired from the University of Chile, care, and monitoring at the University of Talca. The rats were housed under standard environmental conditions ( $22 \pm 2^\circ\text{C}$ , 75–80 % relative humidity, 12-h light/dark cycle). They were weighed at the beginning and end of the experimental period. The animals were fed a standard diet manufactured by Champion, containing 6.4 % moisture, 3.6 % lipids, 6.7 % protein, 7.3 % ash, 3.6 % fiber, and 72.4 % carbohydrates. The rats had *ad libitum* access to food and water, and bedding was changed weekly. Staff maintained a daily record of any changes in behavior or consumption for each cage. The study protocol included the induction of diabetes in the rats by administering low doses of intraperitoneal (I.P.) streptozotocin. The procedure followed Furman's protocol [52]. The rats received a dose of 15 mg/kg of STZ I.P. for five consecutive days. Simultaneously, they were given 10 % sucrose water to prevent lethality from hypoglycemia, which was replaced with regular water on day 6. A non-diabetic control group that did not receive STZ was also included. Glycemic measurements were taken, and rats with blood glucose levels greater than 175 mg/dL were considered diabetic. These rats were then randomized into different study groups. Wound generation followed the method described by Forero O. et al. [41]. Briefly, the surgical procedures were performed by anesthetizing the rats with Ketamine 75 mg/kg, Xylazine 5 mg/kg, and Acepromazine 1 mg/kg. An 8 mm diameter punch biopsy was made at the suprascapular level of the rats. The animals were inoculated with 100  $\mu\text{L}$  of a bacterial culture at  $1 \times 10^{11}$  CFU/mL concentration, grown overnight. The bacterial strains used were *S. aureus* ATCC 25923 and *P. aeruginosa* ATCC 27853. The infection was left to grow for 24 h, and then the groups were given control treatments (mupirocin for *S. aureus* and silver sulfadiazine for *P. aeruginosa*) and the MP-L [I5R8]-loaded DRPHs. The hydrogel was applied only once at the beginning of the treatment and was not replaced during the study. Photographic monitoring of infection progression, wound closure, and temperature control was conducted in all groups on days 1, 8, and 16. The animals were euthanized by an overdose of 150 mg/kg of sodium thiopental anesthetic. After confirming the death by the absence of a heartbeat and palpebral reflex, skin samples were collected and fixed in buffered formalin for a maximum of 24 h before proceeding with various histological protocols.

## 2.8. Histological study

Skin biopsies were obtained from wound closures, and carefully collected using a sterile biopsy punch. The samples were immediately fixed in 10 % formalin (4 % formaldehyde) for 24 h at room temperature. Buffered formalin allowed for the preservation of cellular details and tissue architecture without significant alterations. After fixation, the samples were dehydrated through a series of graded alcohols, cleared in xylene, and embedded in Paraplast (embedding medium Paraplast Plus; melting point: 54 °C; Sigma-Aldrich Chemical Co., St. Louis, MO, USA). Sections with a thickness of 5  $\mu\text{m}$  were prepared using a Leica RM2255 motorized rotary microtome (Leica Microsystems, Switzerland). The sections were then rehydrated, treated with xylene for 10 min, and gradually hydrated through descending concentrations of ethanol (100 %, 96 %, 80 %, and 70 %, each for 15 s), ending with distilled water. Since this is a descriptive study, Hematoxylin-Eosin staining was used. Furthermore, Masson's Trichrome staining was performed to evaluate the arrangement of collagen fibers and the extracellular matrix. Additionally, Sirius red (SR) staining was performed to obtain an accurate characterization of collagen type I and collagen type III fibers revealing the changes in the organization and remodeling of the extracellular matrix during the healing process. For a detailed analysis of histological characteristics, with special attention to structural changes and tissue organization in the injured areas, images were taken using a

Motic Easy Scan Pro® digital scanner (Motic Instrument Inc, Canada) to generate complete panoramic views [42].

## 2.9. Statistical analysis

Each DRPH was produced and characterized in at least three batches. *In vitro* studies included a minimum of three replicates, each involving at least three technical replicates. Results were expressed as mean  $\pm$  standard deviation (SD) or standard error of the mean (SEM). Statistical analysis was carried out in GraphPad Prism 8 software. A p-value  $< 0.05$  was used to connote significance.

# 3. Results and discussion

## 3.1. DRPHs synthesis

NIPAM is a sophisticated material extensively utilized for the fabrication of thermo-sensitive goods owing to its distinctive sol-gel transition characteristics near physiological temperatures [32]. Nonetheless, other modifications of this polymer have been suggested to address specific drawbacks, including rapid collapse due to temperature fluctuations and inadequate biocompatibility, as well as to create HGs with enhanced responsive characteristics appropriate for controlled drug release [37]. This study incorporated comonomers with carboxylic acid functional groups into the pNIPAM chain by free radical polymerization to generate DRPHs that react to both temperature and pH variations (Fig. 1). Hy and Ma were selected as co-monomers due to their pKa values (pKa = 3,96 for Hy, and pKa1 = 1,94 and pKa2 = 6,22 for Ma) at physiological pH, these acids are deprotonated, resulting in a negatively charged polymer [53,54]. This enhances electrostatic interactions with cationic drugs as AMPs, thereby improving the drug release profile from the polymeric matrix. This association is crucial for enhancing peptide retention within the HG, resulting in a prolonged release over time [23].

A preliminary investigation was undertaken to optimize the maximum concentrations of the co-monomers, Hy and Ma, in conjunction with suitable cross-linker concentrations, to ensure the retention of the thermosensitive features of pNIPAM. It was essential to sustain the sol-gel transition temperature within the specified range of 33 °C to 35 °C, without exceeding the temperature necessary for biomedical applications, including wound treatment (Table S2). This was accomplished by meticulously regulating the co-monomer concentration to maintain the HG in a liquid form below 30 °C while guaranteeing it solidifies upon application to a wound [55]. The technique enhances antimicrobial efficacy by extending peptide release, rendering it particularly advantageous for treating bacterial infections. Furthermore, the inclusion of co-monomers enabled the final DRPHs to maintain their injectable solution state at ambient temperature, in contrast to pNIPAM cross-linked alone using cross-linking agents, which resulted in gel formation in the absence of co-monomers (Figure S1). This characteristic significantly enhances the biomedical applicability of DRPHs, particularly for localized treatments such as wound care.

## 3.2. DRPHs characterization

### 3.2.1. FTIR

The DRPHs were synthesized via free radical copolymerization of NIPAM, copolymers (Hy, Ma), and crosslinking agents (PEGDA, and MBA) respectively. FTIR analysis is displayed in Fig. 2. FTIR spectra were obtained for the pure NIPAM monomer, the pNiHyPH and pNi-MaMH, and the MP-L [I5R8]. The spectra were analyzed to identify functional groups, validate the polymerization process, and assess the incorporation of MP-L [I5R8] into the DRPH networks. The FTIR spectrum of pure NIPAM exhibited the N-H stretching from the amide group at 3288  $\text{cm}^{-1}$ , =C-H stretching from the vinyl group at 3071  $\text{cm}^{-1}$ , C-H asymmetric stretching at 2969  $\text{cm}^{-1}$  and C-H symmetric stretching at 2872  $\text{cm}^{-1}$ , C=O stretching from the amide I group at 1680  $\text{cm}^{-1}$ , C=C

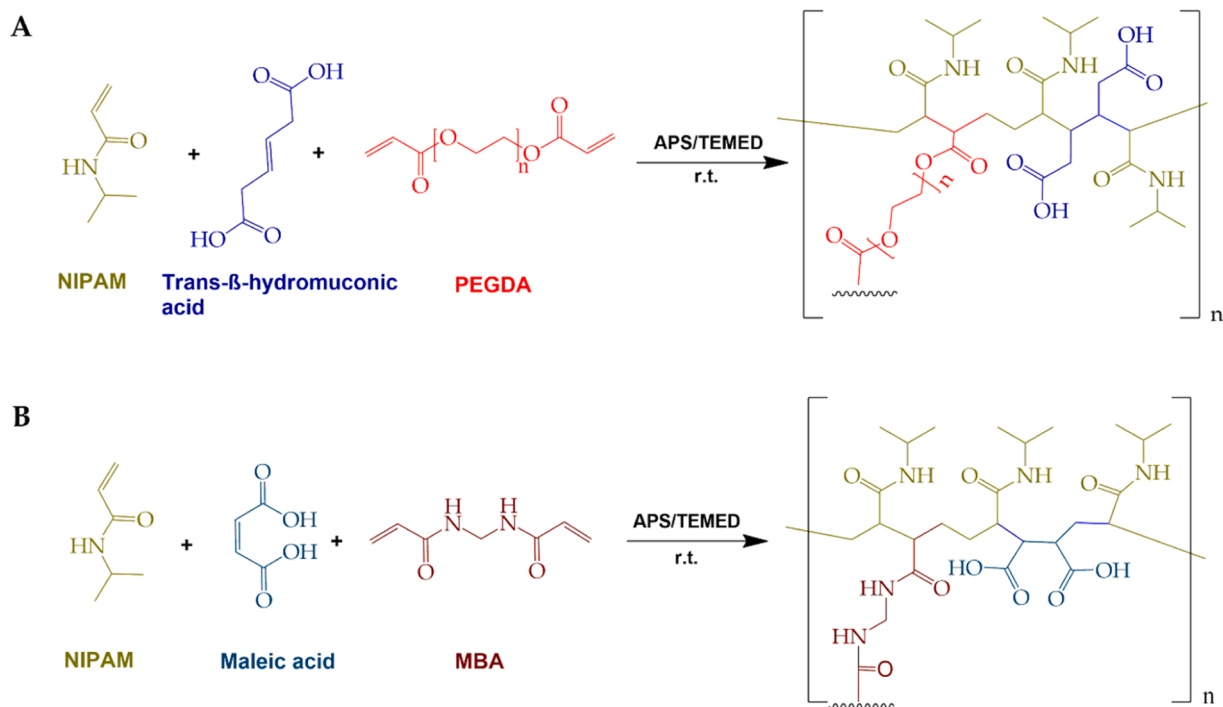


**Fig. 1.** Proposed structure of the DRPHs. pNiHyPH (A) y pNiMaMH (B).

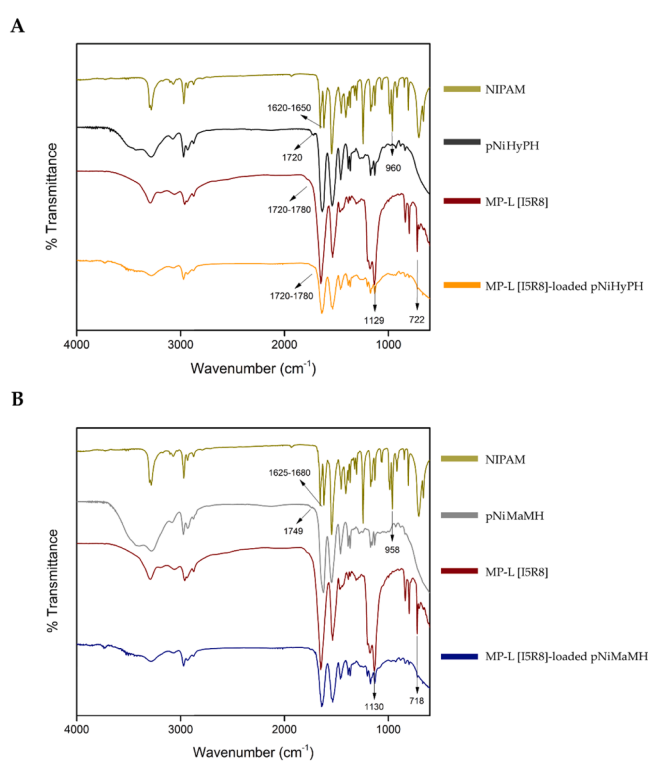


**Fig. 2.** FTIR spectra of pure NIPAM, pure MP-L [I5R8], empty, and MP-L [I5R8]-loaded pNiHyPH (A), and pNiMaMH (B).

aliphatic vibrations at  $1625 \text{ cm}^{-1}$ , N-H bending of the amide II at  $1546 \text{ cm}^{-1}$ ,  $-\text{CH}_2$  bending at  $1454 \text{ cm}^{-1}$ ,  $-\text{CH}_3$  bending at  $1385 \text{ cm}^{-1}$ , C-N stretching at  $1367 \text{ cm}^{-1}$  and  $1244 \text{ cm}^{-1}$ , C-N amide III at  $1170 \text{ cm}^{-1}$ , Vinyl C=C bond bending between  $986$  and  $664 \text{ cm}^{-1}$  [56,57]. For pure MP-L [I5R8], the FTIR spectrum displayed a broad peak from  $3500 \text{ cm}^{-1}$  to  $3286 \text{ cm}^{-1}$  corresponding to the stretching of primary amine (-NH<sub>2</sub>),

secondary amine (R-NH-R), and the amide I band (-CONH<sub>2</sub>). Symmetric stretching of  $-\text{CH}_3$  at  $2964 \text{ cm}^{-1}$  and asymmetric stretching of  $-\text{CH}_2-$  at  $2870 \text{ cm}^{-1}$ , a peak at  $1660 \text{ cm}^{-1}$  corresponding to bending -NH<sub>2</sub> and the amide I band, amide II band and C-N stretching at  $1531 \text{ cm}^{-1}$ , a peak at  $1170 \text{ cm}^{-1}$  corresponding to the dimethyl groups from the leucine residues of the peptide, peaks at  $1130 \text{ cm}^{-1}$  and  $718 \text{ cm}^{-1}$  correspond to the -NH<sub>2</sub> stretching and out-of-plane bending of asparagine and lysine residues, respectively, which were incorporated into both DRPHs. Fig. 2A displays the FTIR spectrum of pNiHyPH, demonstrating the successful polymerization of NIPAM, Hy, and the PEGDA crosslinker. Important spectral data show that NIPAM underwent a conformational change during polymerization. These include a peak shift in N-H stretching from the amide group from  $3288 \text{ cm}^{-1}$  to  $3266 \text{ cm}^{-1}$  and a shift in N-H bending of amide II from  $1546 \text{ cm}^{-1}$  to  $1549 \text{ cm}^{-1}$ . A reduction in the intensity and a shift of the =C-H stretching from the vinyl group (from  $3070 \text{ cm}^{-1}$  to  $3087 \text{ cm}^{-1}$ ), along with the disappearance of the vinyl C=C bond bending (between  $986$  and  $664 \text{ cm}^{-1}$ ), which confirms successful polymerization of NIPAM. O-H stretching shows the presence of carboxyl groups from the Hy comonomer and is characterized by a significant peak between  $3400$  and  $3200 \text{ cm}^{-1}$ . In addition, the existence of a peak at  $1720 \text{ cm}^{-1}$  linked to the C=O stretching of carboxyl groups indicates that Hy has been integrated into the DRPH network. The FTIR spectrum of pNiMaMH is shown in Fig. 2B, which shows that NIPAM, Ma, and the MBA crosslinker were successfully polymerized. During polymerization, NIPAM undergoes structural modifications, as evidenced by the peak shift in the N-H stretching from the amide group from  $3296 \text{ cm}^{-1}$  to  $3272 \text{ cm}^{-1}$  and in the N-H bending of amide II from  $1547 \text{ cm}^{-1}$  to  $1539 \text{ cm}^{-1}$ . The reduction in peak intensity at  $3068 \text{ cm}^{-1}$  from the =C-H stretching of the vinyl group, the shift of C=C aliphatic vibrations from  $1625 \text{ cm}^{-1}$  to  $1686 \text{ cm}^{-1}$ , and the disappearance of the vinyl C=C bond bending (between  $986$  and  $664 \text{ cm}^{-1}$ ) confirm the polymerization of NIPAM monomers. As observed in pNiHyPH, a broad peak between  $3400$  and  $3200 \text{ cm}^{-1}$  corresponds to the O-H stretching of hydroxyl groups from the carboxylic acid of the Ma comonomer. A peak at  $1749 \text{ cm}^{-1}$  corresponds to the C=O stretching of carboxyl groups, indicating the incorporation of Ma into the polymer network.

### 3.2.2 $^1\text{H}$ NMR analysis

Figure S2 presents the  $^1\text{H}$  NMR analysis results for pNiHyPH and pNiMaMH. This data offers comprehensive information on the DRPHs' effective polymerization and structural confirmation. The  $^1\text{H}$  NMR spectrum of pNiHyPH shows characteristic peaks that correspond to the polymerized components of NIPAM, Hy, and PEGDA, confirming the successful synthesis of this DRPH. NIPAM's isopropyl group can be distinguished by a wide peak ( $\text{CH}-(\text{CH}_3)_2$ ) at 1.09 ppm. The primary polymer chain is shown by a wide peak at 1.38 ppm (- $\text{CH}-\text{CH}_2-\text{CH}_2$ ), which forms the backbone of NIPAM. A broad peak (- $\text{CO}-\text{CH}-\text{CH}_2$ ) at 1.95 ppm that is likewise a component of the primary polymer chain. The presence of NIPAM in the polymer matrix is further confirmed by the isopropyl proton at 3.83 ppm (broad,  $\text{CH}-(\text{CH}_3)_2$ ). The primary signal at 2.74 ppm, which corresponds to the proton of the group  $\text{HOOC}-\text{CH}_2-\text{CH}$  identifies the Hy comonomer and verifies its incorporation into the pNiHyPH hydrogel. The C- $\text{CH}_2-\text{O}-\text{C}$  group, which is represented by the PEGDA crosslinker's characteristic signal at 3.64 ppm, denotes successful crosslinking inside the DRPH network. The  $^1\text{H}$  NMR spectrum of pNiMaMH also displays the characteristic peaks of the polymerized components, including NIPAM, Ma, and the MBA crosslinker, confirming its successful synthesis. Similar to pNiHyPH, the isopropyl group of NIPAM in pNiMaMH is observed at 1.09 ppm (broad,  $\text{CH}-(\text{CH}_3)_2$ ). The main chain of NIPAM is represented by a peak at 1.39 ppm (broad, - $\text{CH}-\text{CH}_2-\text{CH}_2$ ) and a peak at 1.95 ppm (broad, - $\text{CO}-\text{CH}-\text{CH}_2$ ). The isopropyl proton of NIPAM also appears at 3.83 ppm (broad,  $\text{CH}-(\text{CH}_3)_2$ ). Ma has been successfully incorporated into the pNiMaMH structure, as evidenced by the signal between 2.75 and 2.77 ppm, which corresponds to the  $\text{HOOC}-\text{CH}-\text{CH}$  protons. A distinctive signal is seen in the MBA crosslinker at 4.70 ppm, which is indicative of the  $\text{HN}-\text{CH}_2-\text{NH}$  protons of the crosslinker. It is important to note that this peak partially overlaps with the  $\text{D}_2\text{O}$  peak [58]. This peak contributes to the crosslinked

network of the pNiMaMH by confirming the existence of an MBA in it.

By integrating the specific peaks, it was possible to determine the ratio of monomer/co-monomer/crosslinker in each DRPH. In the case of pNiHyPH, the peak b is assigned to the isopropyl proton in NIPAM (broad,  $\text{CH}-(\text{CH}_3)_2$ ). Each NIPAM molecule contributes one proton to this peak. The peak f is assigned to the proton from the grafted Hy ( $\text{HOOC}-\text{CH}_2-\text{CH}-$ ). Each PEGDA molecule contributes two protons to this peak ( $\text{C}-\text{CH}_2-\text{O}-\text{C}$ ). Consequently, the integral of peak B (NIPAM) equals ten, indicating the same number of NIPAM molecules. The integral of peaks f corresponds to one proton of a single Hy molecule. The integral of peak e (PEGDA) equals ten, which corresponds to two protons per molecule; therefore, there are five crosslinker molecules. Therefore, the estimative ratio of pNiHyPH is 10:1:5.

In the case of pNiMaMH, the peak b corresponds to the isopropyl proton in NIPAM (broad,  $\text{CH}-(\text{CH}_3)_2$ ). Each NIPAM molecule provides one proton to this peak. The peak g corresponds to the proton from the grafted Ma ( $\text{HOOC}-\text{CH}-\text{CH}-$ ). Each MBA molecule provides two protons to this peak ( $\text{HN}-\text{CH}_2-\text{NH}$ ). As a result, the following integration values were obtained: The integral of peak B (NIPAM) is fifty-five, signifying one proton per NIPAM molecule. The integral of peak g (Ma) is one, indicating the presence of one proton; thus, there is one Ma molecule. The integral of peak e (MBA) equals two, which corresponds to two protons per molecule; therefore, there is one crosslinker molecule. In conclusion, the estimative ratio of pNiMaMH is 55/1/1.

These results correlate with the swelling degree; for example, for pNiHyPH, with a ratio of 10:1:5 for NIPAM, Hy, and PEGDA, suggesting a relatively high crosslinker density. This denser network limits swelling, resulting in a moderate swelling rate of 509 %. In contrast, pNiMaMH shows a ratio of 55:1:1 for NIPAM, Ma, and MBA, reflecting a much lower crosslinker density. This allows for a looser network structure, leading to a significantly higher swelling capacity of 1596 % due to

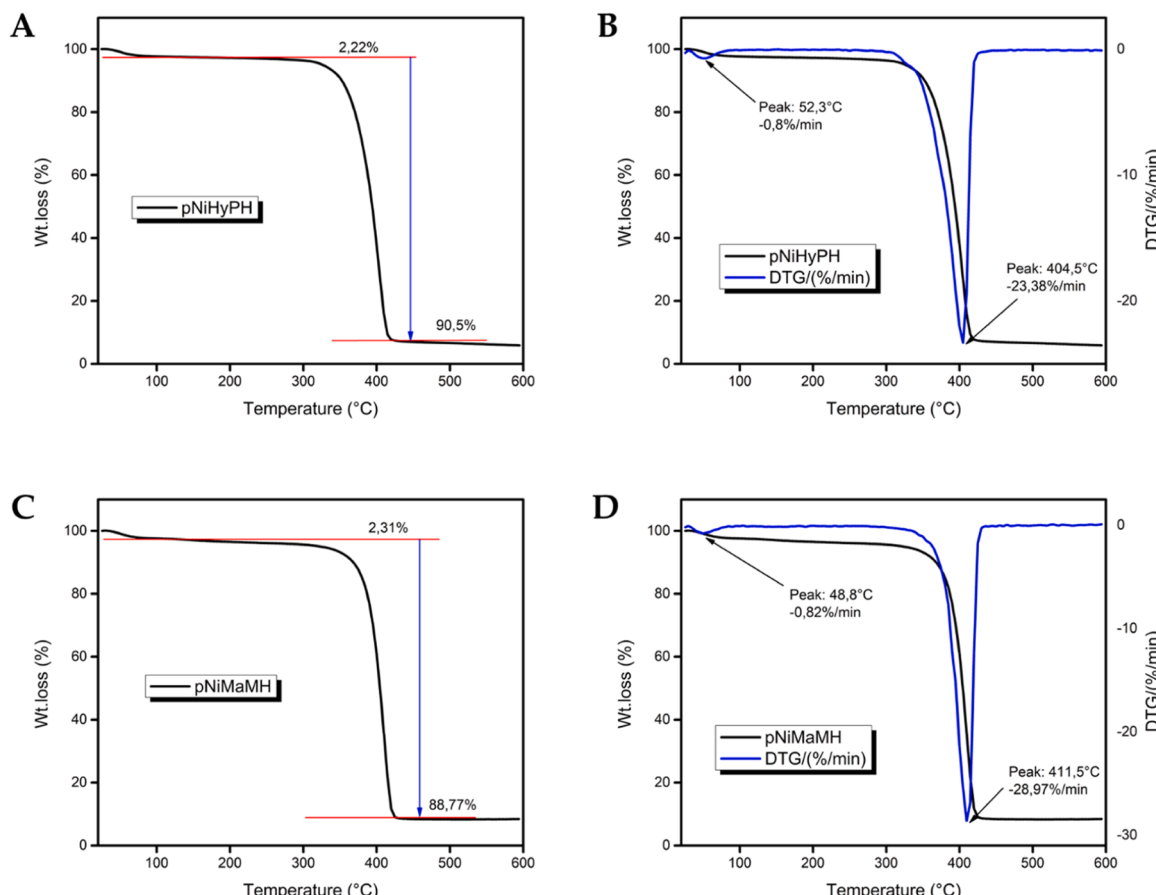


Fig. 3. TGA and DTG spectra of pNiHyPH (A-B), and pNiMaMH (C-D) respectively.

increased water absorption.

### 3.2.3. Thermogravimetric analysis (TGA)

**Fig. 3** includes four TGA graphs with DTG for pNiHyPH and pNiMaMH. These figures provide information about the weight loss of materials as a function of temperature and the rate of weight loss during decomposition. **Fig. 3A** shows the thermal stability of pNiHyPH, a first decomposition is exhibited at 52.3 °C with a slight mass loss of 2.22 % in the early stages, indicating minor volatilization or moisture loss. The major degradation occurs at 404.5 °C leading to a total weight loss of around 90.5 %. The graph reveals that the majority of the degradation occurs after 200 °C, with a significant degradation event visible between 200 °C and 600 °C. **Fig. 3B** compares the TGA and DTG results of pNiHyPH. The initial weight is 100 % and there is minimal weight loss at lower temperatures as indicated by a peak at 52.3 °C, which relates to a minor weight change of 0.80 %/min. The main degradation event occurs between 300 °C and 450 °C, where the sample experiences a mass change of 94.19 %, meaning nearly the entire sample is degraded in this temperature range. The significant weight loss suggests that the material is not stable beyond 300 °C. The major degradation peak occurs at 404.5 °C with a degradation rate of 23.38 %/min, which indicates that this is the temperature at which the sample's thermal degradation rate is highest. **Fig. 3C** shows the thermal stability of pNiMaMH which is similar to **Fig. 3A**, it shows two phases of degradation, a small initial weight loss of 2.31 %. The total weight loss at the end of the measurement is 88.77 %. The degradation rate is similar to pNiHyPH, but the final weight loss is slightly lower. The TGA curve displays the weight loss (%) as a function of temperature. The pNiMaMH (see **Fig. 3D**) starts at 100 % weight with a small initial degradation event occurring at 48.8 °C, corresponding to a slight weight loss of 0.82 %/min. The primary weight loss event occurs between 300 °C and 450 °C, where a mass change of 91.52 % is observed, demonstrating important degradation of the DRPH. Similar to pNiHyPH, most of the weight loss occurs in this temperature range reflecting the thermal stability of prepared DRPHs.

The DTG curve shows the rate of weight loss (%/min) as a function of temperature. The most significant degradation peak occurs at 411.5 °C with a degradation rate of 28.97 %/min. This peak indicates the highest rate of mass loss, suggesting that this is the point where the DRPH experiences the fastest thermal degradation. Finally, in both DRPHs, the early mass loss is mainly attributed to moisture loss (between 50 °C and 100 °C) and both physically weakly adsorbed water and chemically strongly bound adsorbed water (between 100 °C and 180 °C). On the other hand, decomposition events in the 400–500°C region are previously described in the formation of DRPHs [59].

### 3.2.4. Rheological properties

The rheological properties of forming pNiHyPH are observed as a function of temperature by analyzing the shear storage modulus  $G'$  and the loss modulus  $G''$ . The storage modulus  $G'$  represents the elastic component, whereas the loss modulus  $G''$  denotes the viscous aspect of viscoelastic behavior.  $G'$  represents the stored energy, whereas  $G''$  indicates the deformation energy dissipated due to internal friction during shearing [60]. The analysis shows that both  $G'$  and  $G''$  stay low and steady between 25 °C and 30 °C (see **Fig. 4A-I**), which means that the material is in a liquid-like state that is safe for injection at room temperature. As the temperature attains 33–35 °C,  $G'$  markedly increases and surpasses  $G''$ , indicating the transition of pNiHyPH from a liquid to a gel state. The sol-gel transition corresponds with physiological temperatures, enabling the DRPHs to form after injection within the body, which is essential for localized drug delivery. Above 35 °C,  $G'$  increases more significantly than  $G''$ , signifying that pNiHyPH has largely become elastic, maintaining its structure and stability for prolonged therapeutic release. **Fig. 4B-I** illustrates the  $G'$  and  $G''$  as a function of temperature, emphasizing its thermoresponsive features of pNiMaMH. At temperatures ranging from 25 °C to around 30 °C, both  $G'$  and  $G''$  are almost zero, signifying a mostly liquid-like condition. At approximately 33 °C,  $G'$  suddenly increases, exceeding  $G''$  and indicating the commencement of gelation, as the pNiMaMH shifts from a viscous to a more elastic,

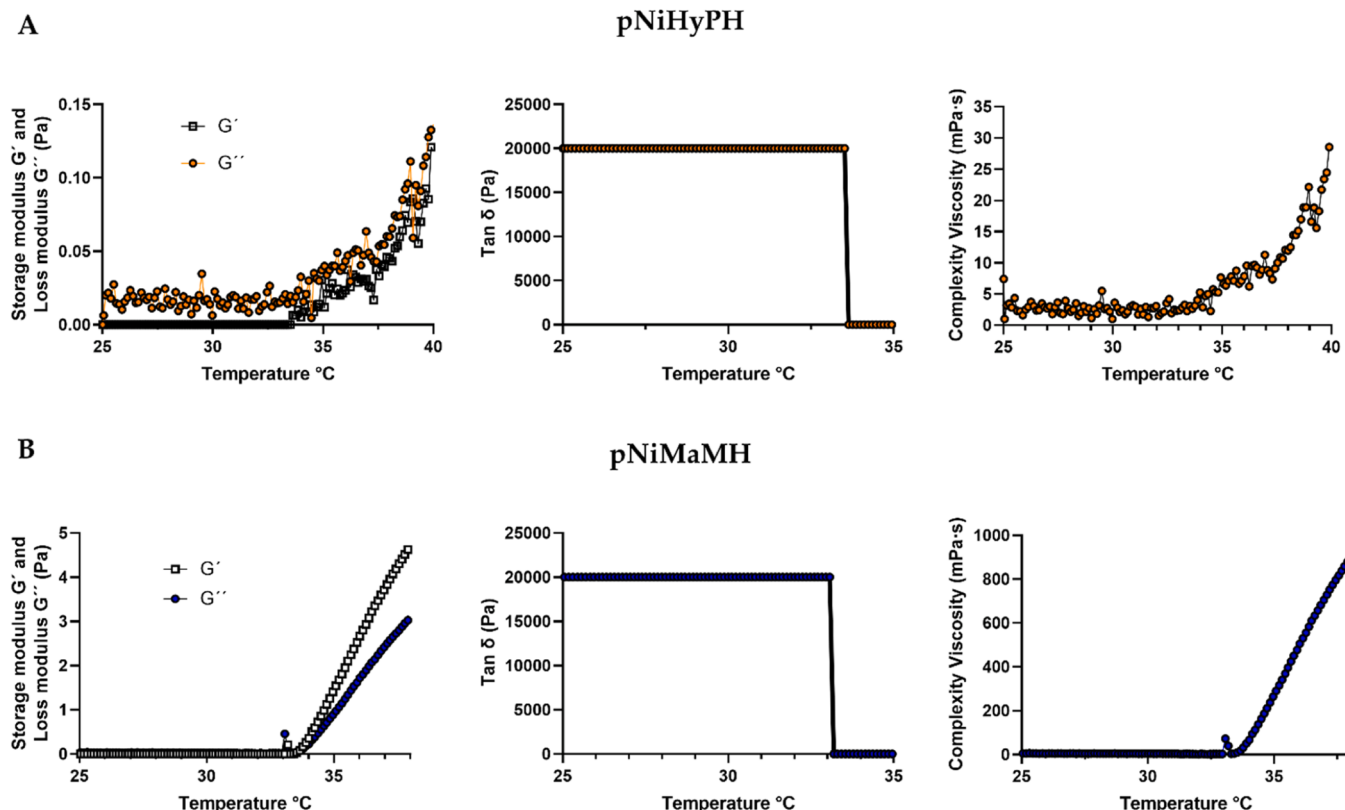


**Fig. 4.**  $G'$  and  $G''$ , loss factor and complex viscosity of hydrogels as a function of temperature. pNiHyPH in A, and pNiMaMH in B.

solid-like condition. The fast increase, especially in  $G'$  at body temperature, shows a strong sol-gel transition that is good for biomedical uses where the pNiMaMH needs to stay liquid for easy injection but harden at body temperature to make localized, long-term drug delivery easier.

In Fig. 4A-II, pNiHyPH stays at a steady loss factor ( $\tan \delta = G''/G'$ ) [61] value of about 20,000 Pa from 25 °C to just below 35 °C. This means that the viscoelastic balance is the same at all temperatures in this range. This stability indicates that the pNiHyPH preserves its structure without substantial alterations until it undergoes a dramatic phase transition at 35 °C, at which point  $\tan \delta$  decreases quickly up to a value less than one. This change means that the pNiHyPH quickly goes from a viscous (like a liquid) state to a solid-like gel state. This is ideal for biomedical uses because the pNiHyPH can be used as a liquid at room temperature and then quickly harden at body temperature. Because of this property, pNiHyPH is good for targeted and long-term drug delivery because it can keep its shape and allow sustained release when it reaches physiological temperatures. In the case of pNiMaMH (see Fig. 4B-II), the loss factor remains consistent at around 20,000 Pa from 25 °C to slightly under 35 °C. This indicates that the viscoelastic characteristics of pNiMaMH remain consistent at these temperatures. Upon reaching a temperature of 35 °C, there is a significant decline in  $\tan \delta$  to nearly zero, indicating a fast phase change from a viscous (liquid-like) state to a solid-like gel state. This abrupt transition aligns with the thermoresponsive properties of the hydrogel, allowing it to remain in a liquid state for facile injection and subsequently harden at physiological temperatures for effective targeted drug delivery. This feature renders pNiMaMH appropriate for applications necessitating fast gelation at physiological temperature to facilitate regulated and prolonged therapeutic release.

Fig. 4A-III illustrates the complex viscosity ( $\eta^*$ ) of pNiHyPH concerning temperature [62]. The viscosity stays low and steady from 25°C to around 30°C, indicating a liquid-like state conducive to injection. At around 33°C, the viscosity increases significantly, indicating the commencement of the sol-gel transition. This increase continues beyond 35 °C, reaching higher viscosity levels, which reflects the hydrogel's transition into a solid-like gel state at physiological temperatures. This thermoresponsive behavior enables pNiHyPH to stay in a liquid state at room temperature for easy administration and then solidify in the body to provide controlled, sustained drug release, making it ideal for localized biomedical applications.

Fig. 4B-III illustrates the complex viscosity of pNiMaMH concerning temperature. Between 25°C and around 30°C, the viscosity approaches zero, signifying a liquid-like state that promotes injection. At around 33 °C, the viscosity markedly escalates, indicating the commencement of the sol-gel transition. The increase persists beyond 35 °C, with viscosity attaining elevated levels, signifying that the hydrogel has shifted to a solid-like gel state at physiological temperatures. As the temperature rises, the viscosity quickly increases. This shows that pNiMaMH is thermoresponsive, which means it can be given as a liquid that quickly solidifies inside the body. This makes it suitable for localized, long-term drug delivery applications.

According to these analyses, the graft of co-monomers was successful because Hy makes the rheological properties of pNiHyPH much better (see Fig. 4 and S3). This is because Hy increases the storage modulus ( $G'$ ), which keeps the structure and elasticity intact. Moreover, stabilizes the loss modulus ( $G''$ ) to minimize extraneous flow, hence maintaining the gel state at physiological temperatures. Also, regulating the sol-gel transition to occur consistently and reliably at around body temperature. Enhancing network density to withstand deformation, guaranteeing extended material efficacy. Finally, it could facilitate a regulated medication release profile by rheological consistency. The rheological properties of Hy are very important for making hydrogels that are meant to deliver drugs locally and for a long time. This is especially true in situations where the gels need to be able to respond to changes in temperature and be more stable mechanically. In the same way, the inclusion of Ma in the pNiMaMH formulation substantially influences its mechanical and functional characteristics (see Fig. 4 and S3). Ma

increases the swelling capacity of pNiMaMH, enabling it to engage with fluids more effectively and promoting an initial, fast drug release. The presence of this co-monomer reduces the cross-linking density, resulting in a more flexible and adaptable network that maintains resilience in dynamic conditions. Ma also helps a sol-gel change happen quickly and clearly at temperatures close to body temperature. This makes sure that the DRPH hardens quickly after injection, which is important for targeted drug delivery applications. The fast gelation makes a dual-phase release profile possible, giving the drug an immediate boost and then a steady, long-lasting release. Because of its rheological properties, pNiMaMH is a great choice for uses that need both immediate localized action and long-term therapeutic release. This is especially true when treating infections in complicated wound settings. The attributes of the flexibility of DRPH, fast gelation, and regulated release augment its efficacy and versatility in biological applications.

In conclusion, the rheological data shows that these hydrogels can be injected while still liquid and hardened at the site of infection, making the MP-L [I5R8] more stable and increasing the rate at which it is released. Because pNiHyPH and pNiMaMH have different networks, they can be used in a variety of therapeutic settings. This means they can be used to treat both short-term and long-term wounds and infections.

### 3.2.5. Scanning electron microscopy (SEM)

The surface morphology and network structure of lyophilized pNiHyPH and pNiMaMH at different temperatures (25 °C and 35 °C) evaluated by electron microscopy are shown in Fig. 5. The pNiHyPH at 25 °C (Fig. 5A) shows a porous structure with distinct differences in magnification across the three images. At higher magnifications, the sample seems to have a fibrous or network-like appearance, indicating a well-developed porous structure. The observed structure suggests that the hydrogel may have a high surface area and could be useful for the sustained release of active compounds such as antimicrobial peptides. In Fig. 5A, pNiHyPH at 35 °C seems to retain its porous structure, though the pores appear more compressed or slightly collapsed compared to the 25 °C sample. There may be some thermal effect that causes slight deformation of the structure as the temperature increases. notwithstanding the above, the overall network structure remains visible and intact.

The pNiMaMH at 25 °C (Fig. 5B) shows a less defined porous structure compared to pNiHyPH, with what seems to be a smoother and denser surface morphology. The surface looks more compact, with fewer distinct pores visible at higher magnifications, which may indicate a different interaction with temperature compared to pNiHyPH. The structure of pNiMaMH at 35 °C appears to expand with more elongated and visible pores compared to the sample at 25 °C. There are more visible channels or networks within the structure suggesting that the material becomes more porous at higher temperatures.

In summary, pNiHyPH displays a highly porous structure that seems to be more stable across both temperatures. At 35 °C, the pores are slightly compressed but maintain their network organization. In the case of pNiMaMH, it showed a more compact structure at 25 °C but it seems to expand at 35 °C displaying a more porous network at the higher temperature. These SEM photos suggest that the DRPHs respond differently to changes in temperature with pNiHyPH maintaining a more consistent structure and pNiMaMH exhibiting significant structural changes in the matrix as the temperature rises. This could indicate differences in their thermal or hydration properties possibly affecting their use in applications like drug delivery, where the response of DRPHs to temperature is critical.

### 3.2.6. Gelation time and temperature, and swelling degree

The degree of swelling of the prepared DRPHs was assessed (Fig. 6B), reaching equilibrium in less than eight hours—a typical occurrence for NIPAM-based hydrogels [44]. The findings reveal a significant difference in the swelling capacities of the two DRPHs: pNiHyPH swells at a rate of 509 %, whereas pNiMaMH achieves a swelling percentage of

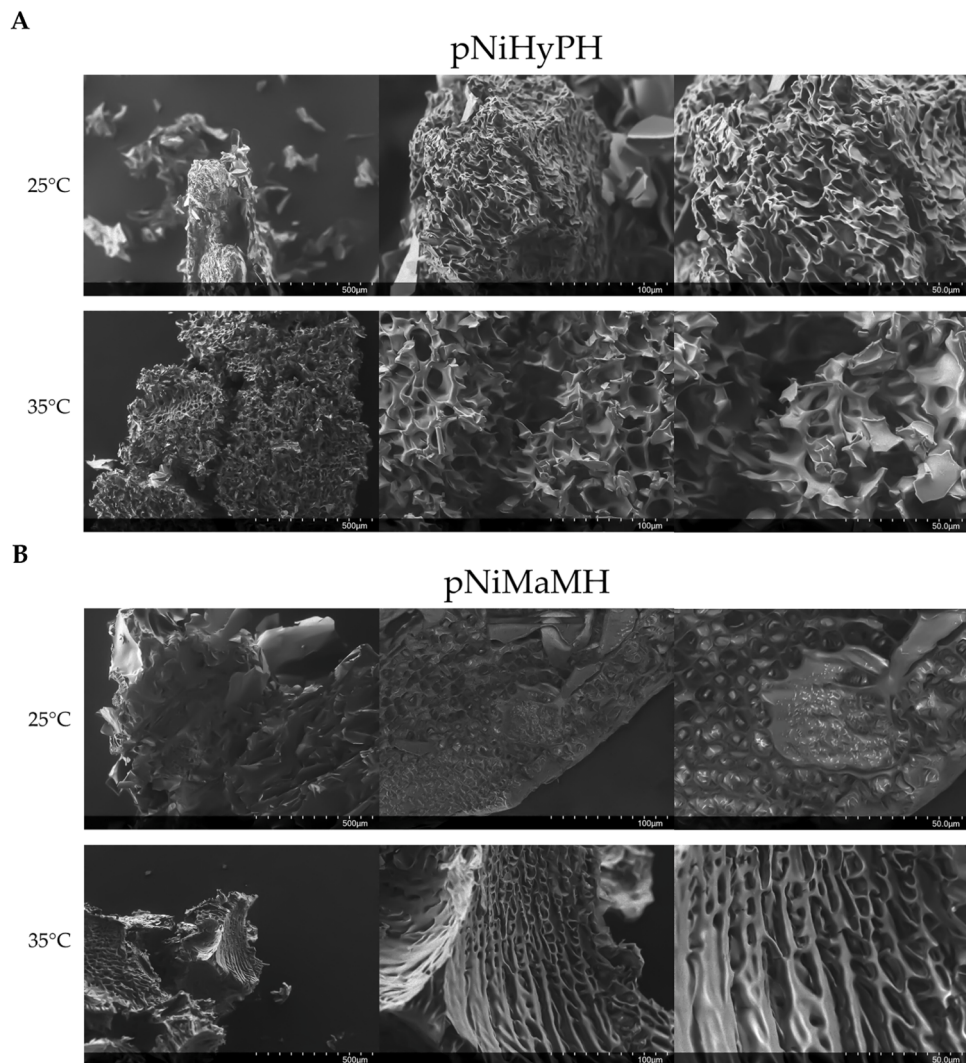


**Fig. 5.** Hydrogels morphologic characterization. DRPHs at 25° and 35 °C at different magnifications: 100x, 500x and 1000X. pNiHyPH (A) and pNiMaMH (B).

1596 %. This notable variation is largely attributed to differences in both the crosslinking agents and co-monomers used in each DRPH.

**Fig. 6** shows the physicochemical properties of the DRPHs, including their swelling capacity and phase change behavior. Turbidimetric data were used in the phase change investigation (**Fig. 6A**) to assess how temperature affected both hydrogels. The sol-gel transition for both pNiHyPH and pNiMaMH starts at about 30 °C, which is good for injectable applications because it stops gelation at lower temperatures. In particular, pNiHyPH displays a sol-gel transition temperature of 33.5 °C, whereas pNiMaMH displays a temperature close to physiological levels, 34.1 °C. This behavior guarantees that the DRPHs stay liquid during administration but gel when they reach body temperature, which is important for *in vivo* applications.

The choice of crosslinking agent plays a crucial role in influencing the swelling capacity. A higher incorporation of PEGDA, as compared to MBA, results in a more flexible and less dense network structure. This increased flexibility enhances swelling potential by providing additional space for water absorption within the hydrogel, an advantage particularly valuable for applications requiring high fluid retention, such as drug delivery systems or wound healing. In addition to the crosslinking agents, the co-monomers contribute to the swelling differences observed. Hy, with a low water solubility of 17 g/L, limits hydrophilic interactions in pNiHyPH, reducing its swelling relative to the control hydrogel without Hy (**Figure S4** and **Table S3**). Conversely, Ma, incorporated into pNiMaMH, has a much higher water solubility ( $\geq 100$  g/L),

which promotes hydrophilic interactions and significantly increases the swelling capacity of pNiMaMH relative to the control hydrogel without Ma (**Figure S4** and **Table S3**).

In pNiHyPH, although the crosslinker PEGDA is normally hydrophilic, the less soluble Hy component might have a greater impact on swelling. The DRPHs mechanical characteristics are also influenced by the crosslinker MBA. In comparison to PEGDA, MBA usually offers a more rigid structure, which may help the DRPH maintain its structural integrity during swelling and encourage even more water absorption [63]. Because Ma is included, pNiMaMH can expand much more than pNiHyPH because it encourages more extensive hydrophilic interactions with water molecules. Compared to pNiHyPH based on Hy, the polymer can swell to a far greater extent due to the enhanced solubility and carboxyl functionality of Ma [64].

These variations in swelling behavior also imply that the two DRPHs release profiles differ. In contrast to pNiMaMH, which may release pharmaceuticals more quickly due to its higher swelling and fluid absorption capacities, HGs such as pNiHyPH, which have a lesser swelling capacity, may provide a more regulated and sustained drug release [44].

The thermoresponsive activity of DRPHs is visibly confirmed in **Fig. 6C**, wherein both pNiHyPH and pNiMaMH stay in a solution state at 25 °C but change to a gel state at 35 °C. This sol-gel transition at body temperature is a key property for *in situ* gelling applications, ensuring that the DRPHs may be easily injected at ambient temperature but will solidify upon reaching physiological conditions.

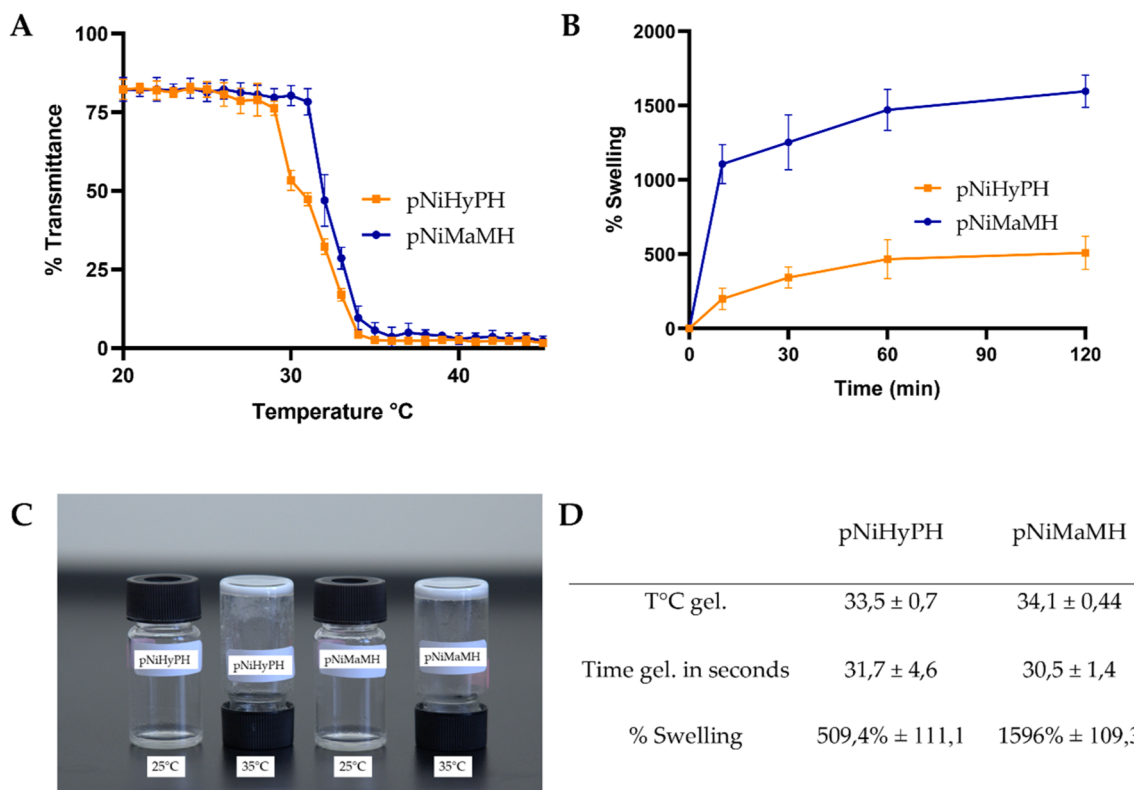


**Fig. 6.** Phase change study of DRPHs by turbidimetric determination (A), determination of the swelling percentage of DRPHs (B), the image of pNiHyPH and pNiMaMH in liquid state at 25 °C and in gel form at 35 °C (C), and summary table with physical characteristics of the DRPHs (D).

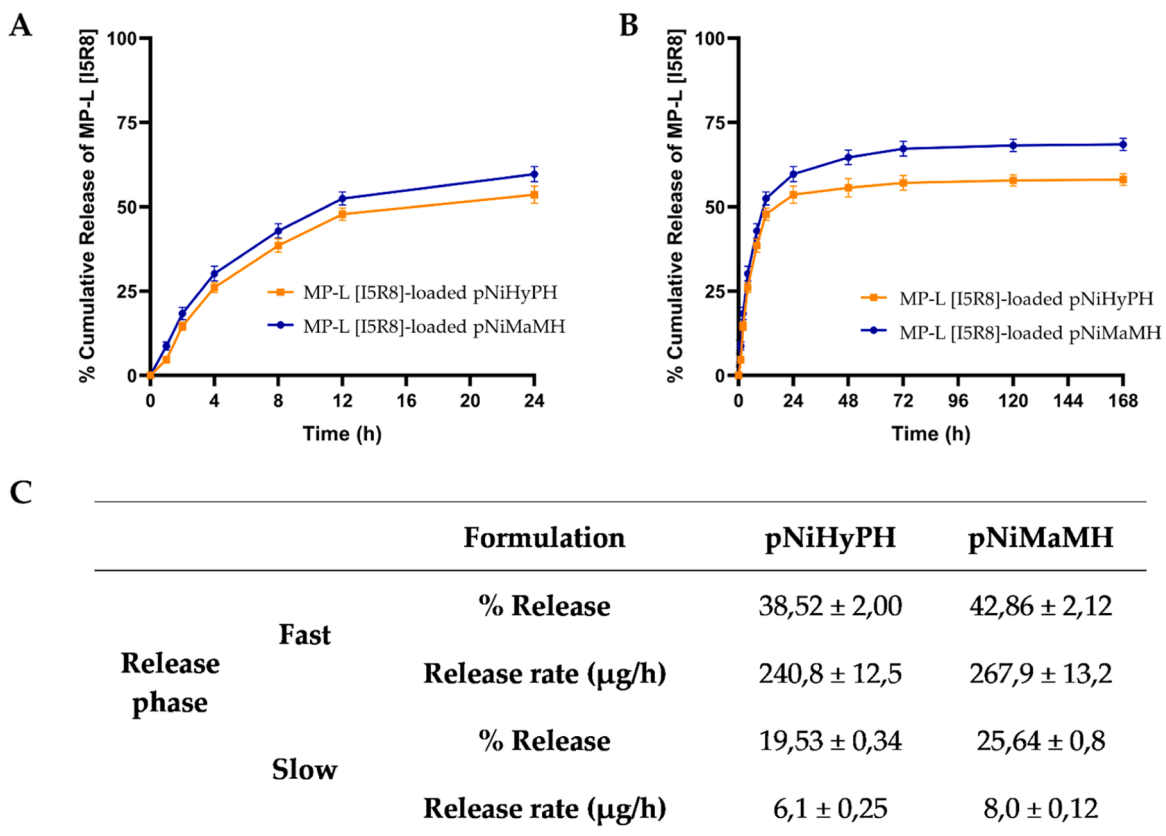


**Fig. 7.** *In vitro* MP-L [I5R8] release profile from DRPHs. Release kinetic from pNiHyPH and pNiMaMH at 24 h (A) and 168 h (B). Release phases of MP-L [I5R8] from the DRPHs (C).

Lastly, Fig. 6D presents a summary of the findings, indicating that the two DRPHs physical characteristics differ from one another. The gelation temperature, gelation time, and swelling capacity of pNiHyPH are  $33.5 \pm 0.7$  °C,  $31.7 \pm 4.6$  s and  $509.4 \% \pm 111.1$ , respectively. On the other hand, pNiMaMH exhibits a significantly larger swelling capacity of  $1596 \% \pm 109.3$ , a faster gelation time of  $30.5 \pm 1.4$  s, and a gelation temperature of  $34.1 \pm 0.44$  °C.

In conclusion, both pNiHyPH and pNiMaMH exhibit thermoresponsive behavior, making them appropriate for biomedical applications where temperature-induced gelation is necessary. Though pNiHyPH might be more appropriate for applications needing a more regulated release of therapeutic chemicals, pNiMaMH's larger swelling capacity makes it a better option for those requiring extensive fluid absorption, such as wound care. These results demonstrate the DRPHs adaptability and their potential for specialized applications in wound healing and medication delivery systems.

### 3.3. Release kinetics profile of MP-L [I5R8]

The cumulative release profiles of MP-L [I5R8] from pNiHyPH and pNiMaMH, were evaluated over time to assess both short-term and long-term release behaviors. Fig. 7A offers a detailed view of the cumulative release data for the first 24 h, while Fig. 7B presents the overall release profile from 0 to 168 h. It is important to note that Fig. 7A is a zoomed-in version of Fig. 7B, focusing specifically on the initial 24 h of cumulative release data. Furthermore, Fig. 7C summarizes key quantitative parameters, including the release percentages and rates during both the fast and slow-release phases for each DRPHs.

As portrayed in Fig. 7A, which zooms in on the initial 24 h of data (short-term release behavior) the release of MP-L [I5R8] from both DRPHs follows a different pattern throughout the early stages. pNiMaMH exhibited a faster release of MP-L [I5R8] achieving around 60 % cumulative release within 24 h, whereas pNiHyPH released nearly 50 % over the same period. This difference in release rates suggests that pNiMaMH facilitates a more rapid diffusion of MP-L [I5R8] during the initial hours. The magnified view of the first 24 h provided by Fig. 7A highlights these early differences, offering a more detailed perspective on the initial release behavior of each DRPHs.

In the extended period of 168 h or long-term release behavior (see Fig. 7B), both DRPHs continue to release MP-L [I5R8] but with visible differences in their overall profiles. pNiMaMH preserves a higher cumulative release, reaching close to 70 % by the end of the analysis, while pNiHyPH lags slightly behind with an approximate 60 % release. The gradual and sustained release from both DRPHs denotes that they can be effective in providing extended release over time, although pNiMaMH releases more MP-L [I5R8] overall, suggesting better long-term performance in drug delivery.

Additionally, the release profile of MP-L[I5R8] from both DRPHs at different pH levels was studied, as shown in Figure S5. Although pH is dynamic during an infection, various clinical studies report an approximate range of 6–8, depending on the stage of the disease (chronic or acute). Moreover, pH can vary further depending on the infectious agent [65–68]. In this context, for both synthesized DRPHs, the carboxylic acid comonomers have a pKa value close to 4 [53,54]. Therefore, at pH levels above 6, the -COOH groups are mostly deprotonated, resulting in no statistically significant differences in the peptide release profiles.

The release kinetics were further analyzed in terms of two different phases (see Fig. 7C), the first one is the fast-release phase (early hours) and the second one is the slow-release phase (later hours). During the fast phase, pNiMaMH released  $42.86 \% \pm 2.12$  of MP-L [I5R8], with a release rate of  $267.9 \pm 13.2$  µg/h, outperforming pNiHyPH, which released  $38.52 \% \pm 2.00$  with a slower rate of  $240.8 \pm 12.5$  µg/h. This data confirms the rapid initial release observed in Fig. 7A.

During the slower, prolonged phase (slow-release phase), pNiMaMH continued to demonstrate superior release behavior, with  $25.61 \% \pm 0.48$  of MP-L [I5R8] being released at a rate of  $8.0 \pm 0.12$  µg/h,

compared to  $19.53 \% \pm 0.34$  and  $6.1 \pm 0.25$  µg/h for pNiHyPH. This suggests that pNiMaMH not only releases MP-L [I5R8] faster in the early phase but also sustains release at a higher rate over a longer period.

The data presented highlights the differences in release behavior between the two DRPHs. pNiMaMH reliably outperformed pNiHyPH in both the fast and slow-release phases making it a better candidate for applications requiring both an immediate and sustained release of MP-L [I5R8]. Thus, its capacity to achieve a higher cumulative release over time and a quicker initial release rate indicates that pNiMaMH could be ideal for therapies that require quick onset followed by prolonged drug availability. By contrast, pNiHyPH presents a more sustained release, that could be useful in situations where a slower release of the MP-L [I5R8] is desired to preserve therapeutic levels during an extended period. Therefore, pNiHyPH could be better suitable for circumstances where a reduced frequency of administration is needed.

The release rate of MP-L [I5R8] from the pNiHyPH and pNiMaMH was investigated by exploiting several kinetic models to understand better the mechanisms driving the release process. Table 2 summarizes the rate constants (K), diffusion exponents (n), and regression values ( $R^2$ ) for several models: Zero Order, First Order, Hixson-Crowell, Higuchi, and Korsmeyer-Peppas. Zero-order kinetics suggest that the MP-L [I5R8] release rate is independent of its concentration. However, the  $R^2$  values for both formulations are quite low—0.4512 for pNiHyPH and 0.4987 for pNiMaMH—indicating that the release of MP-L [I5R8] does not follow zero-order kinetics. The rate constants (K) for pNiHyPH and pNiMaMH are 0.2677 and 0.3191, respectively, but the poor fit to the model suggests that this isn't the dominant release mechanism. First-order kinetics assumes that the release rate is proportional to the remaining drug. Again, the  $R^2$  values are relatively low, with pNiHyPH at 0.2898 and pNiMaMH at 0.3542, implying that first-order kinetics do not adequately explain the MP-L [I5R8] release from these DRPHs. Remarkably, the release rate constants (K) for both DRPHs are similar (0.0077 and 0.0072, respectively), however, these values further emphasize that first-order kinetics aren't the main driver of the release process. The Hixson-Crowell model accounts for changes in surface area as particles dissolve. The  $R^2$  values here are also quite low—0.2797 for pNiHyPH and 0.2888 for pNiMaMH—indicating that surface area changes are not a major factor in the MP-L [I5R8] release. The negative rate constants (K = -0.012) further support this conclusion, as they suggest that surface area reduction does not play a significant role in these DRPHs. The Higuchi model is used to describe diffusion-controlled drug release from a polymeric matrix and showed a better fit for both DRPHs. The  $R^2$  values were 0.6917 for pNiHyPH and 0.740 for pNiMaMH, indicating that diffusion plays a significant role in MP-L [I5R8] release particularly for pNiMaMH. The rate constants (K) were 2.1748 and 2.5513 for pNiHyPH and pNiMaMH, respectively, further suggesting that diffusion is a principal mechanism, particularly for pNiMaMH. The Korsmeyer-Peppas model is used for polymer-based formulations where the release mechanism may involve both diffusion and polymer relaxation, providing the best fit for both DRPHs. The  $R^2$  values were 0.8999 for pNiHyPH and 0.9405 for pNiMaMH, indicating that this model describes the MP-L [I5R8] release behavior quite accurately. The rate constants (K) for pNiHyPH and pNiMaMH were 5.47646 and 3.53997, respectively. Moreover, the diffusion exponents (n) were 0.7435 for pNiHyPH and 0.6034 for pNiMaMH, suggesting that the release mechanism is non-Fickian or anomalous, involving both diffusion and matrix relaxation. In conclusion, among the models verified, the Korsmeyer-Peppas model gave the best results, as evidenced by the highest  $R^2$  values. These data suggest that the MP-L [I5R8] release profile from both DRPHs involves a blend of diffusion and matrix swelling or relaxation. The differences in the rate constants and diffusion exponents between pNiHyPH and pNiMaMH reveal that while both DRPHs exhibit similar mechanisms of release, pNiMaMH could offer slightly more controlled and predictable release behavior. The Higuchi model also showed a reasonably good fit, particularly for pNiMaMH, indicating that diffusion is an important aspect of MP-L [I5R8] release in

**Table 2**

MP-L [I5R8] rate constants, diffusion exponent, diffusion types, and regression values in various media for different kinetic models of prepared DRPHs.

Model	Zero Order		First Order		Hixon-Crowell		Higuchi		Korsmeyer-Peppas		
	R <sup>2</sup>	K	R <sup>2</sup>	K	n						
pNiHyPH	0.4512	0.2677	0.2898	0.0077	0.2797	-0.012	0.6917	2.1748	0.8999	5,47646	0.7435
pNiMaMH	0.4987	0.3191	0.3542	0.0072	0.2888	-0.012	0.74	2.5513	0.9405	3,53997	0.6034

these DRPHs.

### 3.4. Biocompatibility assays

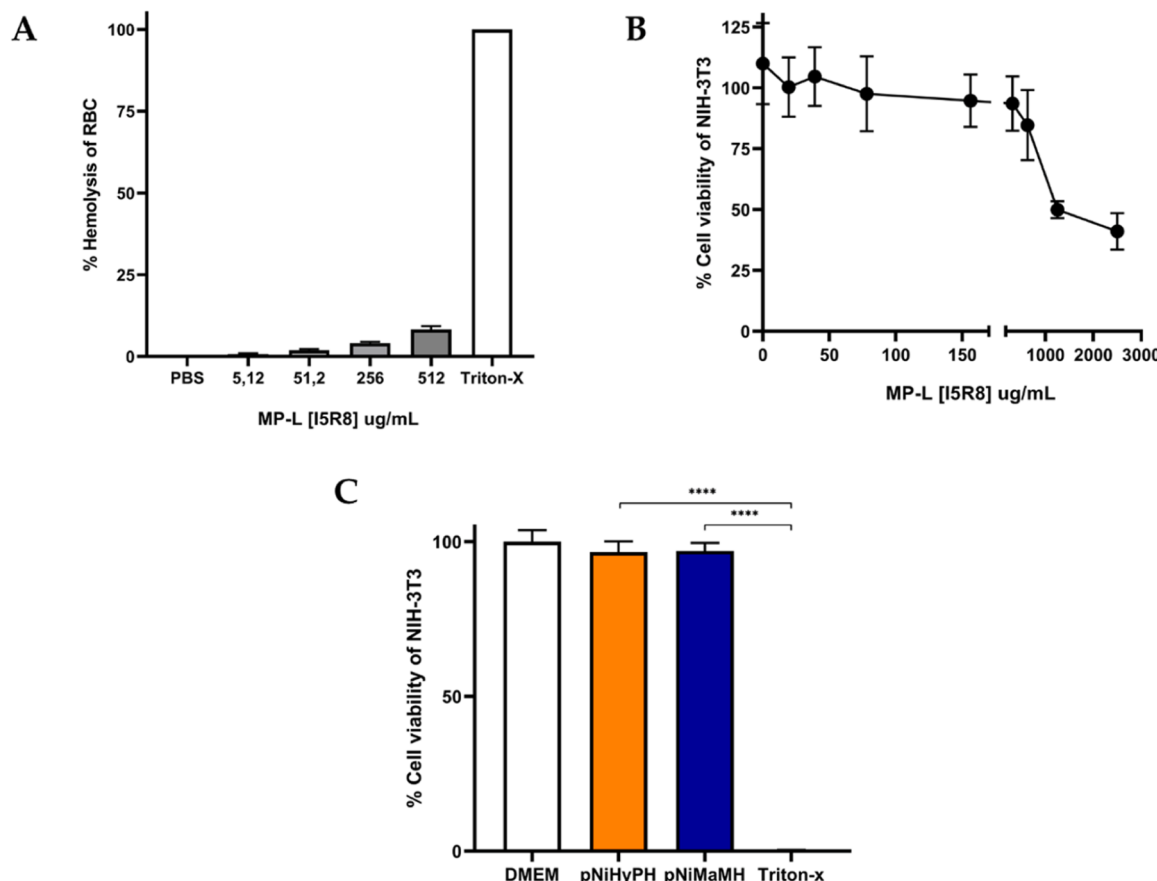
Fig. 8A displays the percentage of hemolysis detected when RBCs were treated with different concentrations of MP-L [I5R8] (0.5–512 µg/mL) compared to the negative control (PBS) and the positive control (Triton-X). The hemolysis degree across MP-L [I5R8] concentrations appears insignificant, remaining well below 5 %, suggesting that the peptide, even at high concentrations, induces minimal hemolysis. However, Triton-X exhibits almost 100 % hemolysis, which is to be expected from an agent that disrupts membranes. These data show that, at the observed doses, the MP-L [I5R8] has limited hemolytic potential and is not likely to substantially injure red blood cells. The concentration at which the peptide could cause 50 % RBC hemolysis (LC50) was obtained, which was 3439 µg/mL, this was determined by extrapolating the results obtained in the hemolysis assay (Table S4).

Fig. 8B shows the dose-response curve for the viability of NIH-3T3 cells in response to increasing MP-L [I5R8] concentrations as determined by the MTT assay. Cell viability is nearly constant at low dosages (up to 1000 µg/mL), indicating minimal cytotoxic effects. Cell viability,

however, begins to decrease at doses more than 1000 µg/mL. The half-maximal inhibitory concentration (IC50) of MP-L[I5R8] on NIH-3T3 cells corresponds to 1642 µg/mL (Figure S6) and continues to decrease at higher concentrations (2000–3000 µg/mL) (Table S5). These results indicate that MP-L [I5R8] is cytotoxic to NIH-3T3 cells at higher concentrations, with a notable reduction in cell viability observed as the concentration increases beyond 1000 µg/mL. Fig. 8C compares the cell viability of NIH-3T3 cells after treatment with pNiHyPH and pNiMaMH, coupled with the positive control and the negative control. The results show that both DRPHs preserve a high percentage of viable cells—roughly 95 %—which indicates low levels of cytotoxicity. Triton-X caused a sharp decline in cell viability that was almost 0 %, revealing its expected toxic effect. The prepared DRPHs biocompatibility is highlighted by statistical analysis, which reveals significant differences between the DRPHs-treated groups and the Triton-X group but no significant changes between the DRPHs and the negative control.

### 3.5. In vitro antibacterial activity of MP-L [I5R8]—loaded DRPHs

*S. aureus* ATCC 25923 and *P. aeruginosa* ATCC 27853, two of the most frequently isolated bacterial species in complex wound infections such



**Fig. 8.** Biocompatibility assays of MP-L[I5R8] and DRPHs. Hemolysis assay of the peptide on RBC (A), cell viability assessment of the peptide on fibroblasts (B), and cell viability assessment of pNiHyPH and pNiMaMH in fibroblast cell lines (C).

as diabetic foot ulcer infections (DFUIs), were used in the antibacterial activity testing of MP-L [I5R8]. Due to their well-known high levels of acquired resistance (*S. aureus*) and intrinsic resistance (*P. aeruginosa*), these bacteria pose serious problems for the management of wound care [69,70]. MP-L [I5R8]'s MIC and MBC were assessed concerning the two bacterial strains (Fig. 9A and 9B). *S. aureus* and *P. aeruginosa* were reported to have MICs of 32 µg/mL and 16 µg/mL, respectively, for MP-L [I5R8]. These outcomes agree with earlier research by Irazazabal et al [20]. With 40 µg/mL for *S. aureus* and 20 µg/mL for *P. aeruginosa* the MBC values were marginally higher and almost matched the MIC values. The close relationship between MIC and MBC validates the bactericidal properties of MP-L [I5R8], possibly due to its α-helix peptide structure, which enables efficient damage to bacterial cell membranes. MP-L [I5R8] has been shown to cause membrane permeabilization and depolarization, as previously reported by Irazazabal et al., who demonstrated these effects in *E. coli* ATCC 25922 and *S. aureus* ATCC 25923 [20,71,72]. Though with differing kinetics, the time-kill assay (Fig. 9C) demonstrated that MP-L [I5R8] acts quickly against both bacteria. For *S. aureus*, a concentration of MP-L [I5R8] equal to double the MIC was able to kill the bacterium within 20 min, demonstrating fast bactericidal action. In contrast, even though *P. aeruginosa* had a lower MIC and MBC than *S. aureus*, it took it more time to kill—roughly 60 min. The bacterial resistance mechanisms of *P. aeruginosa* may be responsible for the prolonged time it takes to kill bacteria, as they probably reduce the peptide's bactericidal efficacy even at lower doses [73]. These findings are essential for comprehending the antibacterial activity shown in similar patterns of bacterial inhibition in both *in vitro* and *in vivo* release experiments.

The intrinsic antibacterial activity of pNiHyPH and pNiMaMH was assessed alongside MP-L[I5R8]-loaded DRPHs using the agar diffusion test (Fig. 9D). The fact that unloaded DRPHs (devoid of MP-L[I5R8]) did not significantly inhibit bacterial growth suggests that the peptide alone is responsible for the antibacterial activity. In contrast, MP-L[I5R8]-loaded DRPHs exhibited distinct inhibitory zones, indicating the peptide's release and effectiveness. These findings highlight the potential of DRPHs as efficient antibacterial peptide delivery systems for wound care applications.

The effectiveness of MP-L [I5R8] at different concentrations is further supported by the screening for bacterial growth inhibition (Fig. 9A). Near-complete suppression was observed in both *S. aureus* and *P. aeruginosa* bacterial strains at high MP-L [I5R8] doses (512–128 µg/mL). Bacterial growth increased as the concentration dropped, with *P. aeruginosa* showing greater resistance at lower doses than *S. aureus*. Significant bacterial inhibition in both strains was shown to require a concentration of 64 µg/mL; beyond this, particularly at 16 µg/mL and below, the efficiency decreased.

The outcomes of *in vitro* antibacterial activity assays utilizing aliquots taken at various times from the MP-L [I5R8] sustained release study from pNiHyPH and pNiMaMH are shown in Fig. 10. Two prevalent bacteria seen in complex wound infections, *S. aureus* ATCC 25923 and *P. aeruginosa* ATCC 27853, were the targets of these tests. The studies show that, in contrast to administering the peptide in a single dose, DRPH-based methods can provide a protracted release of MP-L [I5R8]. To evaluate the antibacterial activity of the aliquots taken from the release test at various times, the Kirby-Bauer agar diffusion method was used (see Fig. 10A). Wells were created in agar plates seeded with *S. aureus* and *P. aeruginosa*, and aliquots from the release assays were dispensed into these wells. Both pNiHyPH and pNiMaMH loaded with MP-L[I5R8] exhibited a strong and sustained bacterial growth inhibition effect over 168 h, demonstrating the preservation of activity despite exposure to conditions mimicking physiological pH and salinity. In contrast, other mastoparan-derived peptides reported in the literature have a half-life of less than 12 h under physiological conditions [68]. Both DRPHs showed growing inhibitory zones in the early assay hours, indicating a potent antibacterial activity. Moreover, the inhibitory zones continued to be effective after 168 h, demonstrating the long-term antibacterial efficacy of both DRPHs. On the other hand, a substantial initial inhibitory zone was observed following the single-dose injection of MP-L [I5R8], although this diminished considerably after 8 h because of the absence of continuous release. The benefits of prolonged peptide release from DRPHs were highlighted by the fact that the effectiveness of the single-dose treatment decreased as the peptide concentration decreased. In Fig. 10B, the single-dose control loses its effectiveness after 8 h, as evidenced by a sharp decline in the inhibition zone diameter. In

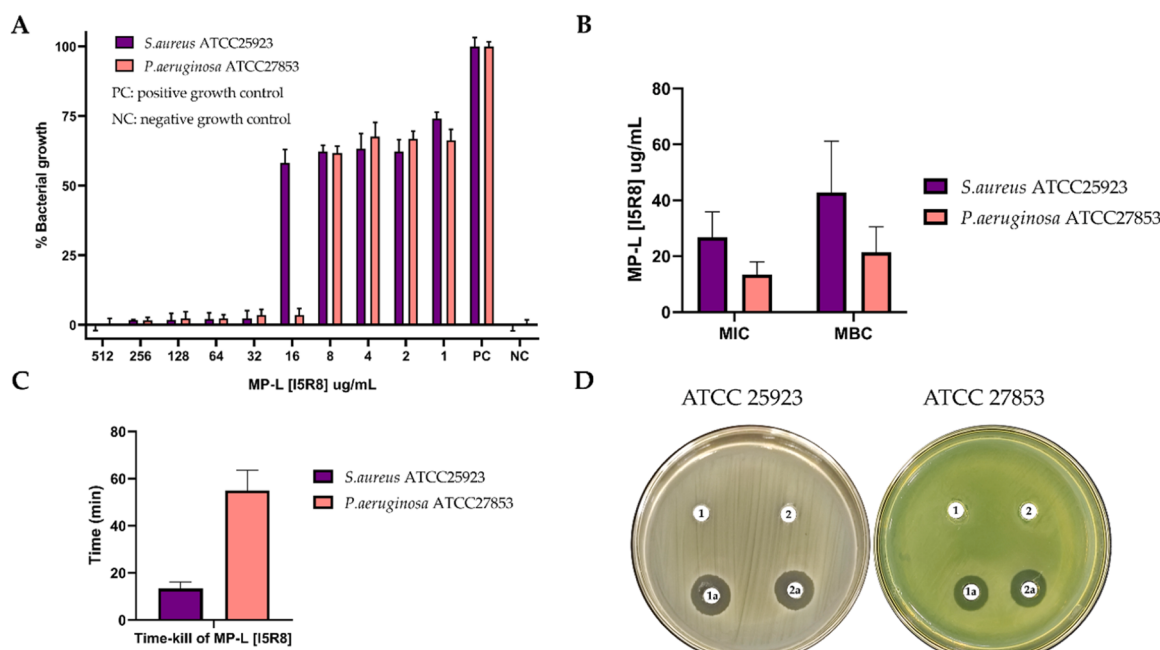


**Fig. 9.** *In vitro* antibacterial activity assays of MP-L [I5R8] and DRPHs against bacterial strains of *S. aureus* ATCC 25923 and *P. aeruginosa* ATCC 27853. Antibacterial activity of MP-L [I5R8], in (A) MIC determination, in (B) MBC determination, and in (C) Time-kill evaluation. In (D) empty pNiHyPH and pNiMaMH (1 and 2), and both hydrogels loaded with 1 mg/mL of MP-L [I5R8] (1a and 2a) against *S. aureus* ATCC 25923 and *P. aeruginosa* ATCC 27853.

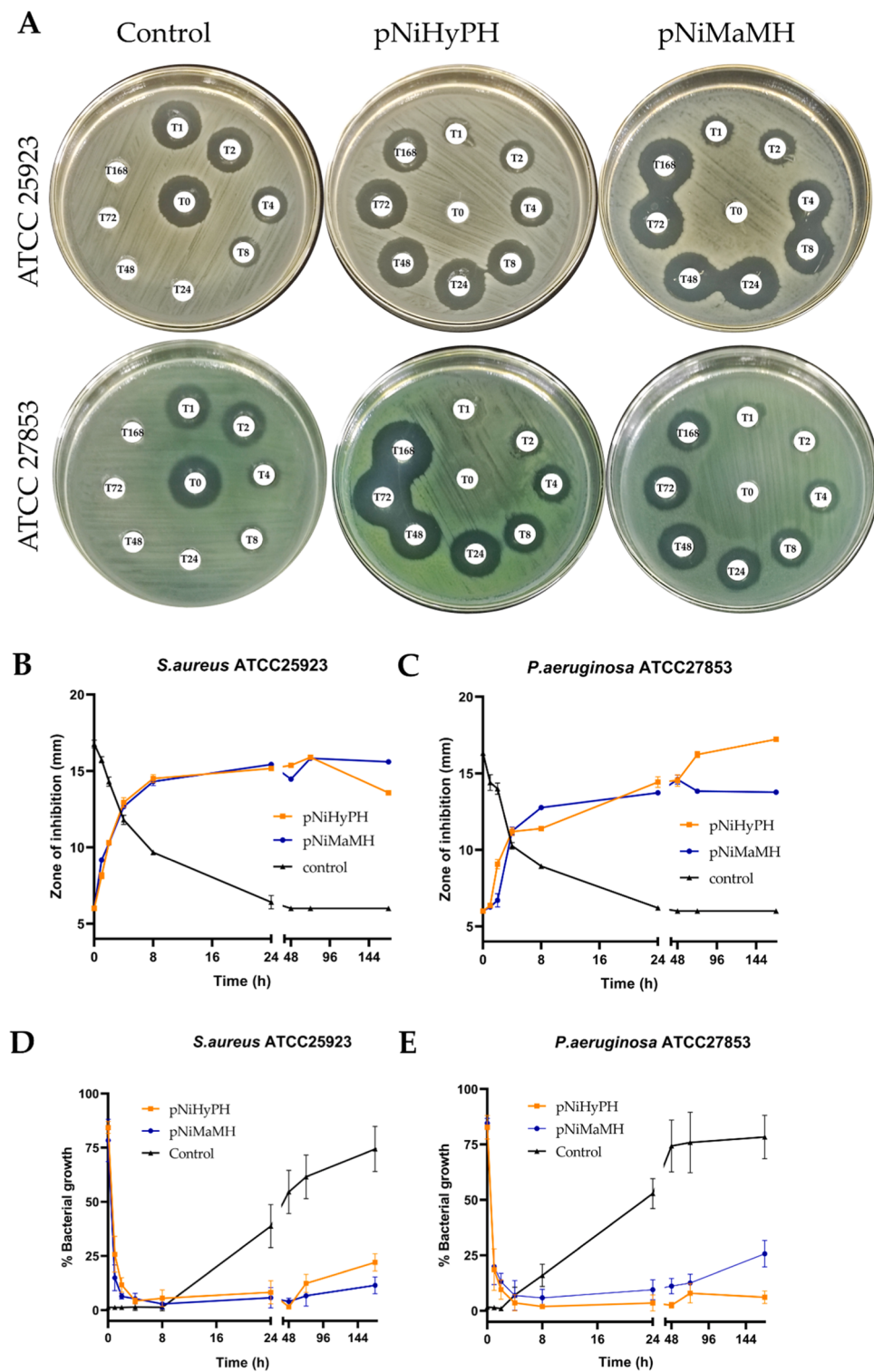


**Fig. 10.** Determination of the in vitro antibacterial activity of the MP-L—loaded DRPHs. Antibacterial effect of the aliquots obtained from the MP-L [I5R8] release assay from the DRPHs over time, compared with the conventional treatment (A). T0: 0 h, T1: 1 h, T2: 2 h, T4: 4 h, T8: 8 h, T24: 24 h, T48: 48, T72: 72 h, T168: 168 h, against *S. aureus* ATCC 25923 and *P. aeruginosa* ATCC 27853. Determination of the inhibition diameter by the Kirby-Bauer diffusion technique of the aliquots of both hydrogels compared with the control treatment against *S. aureus* ATCC 25923 (B) and *P. aeruginosa* ATCC 27853 (C). Determination of bacterial growth inhibition by 96-well microplate assay of aliquots obtained from pNiHyPH and pNiMaMH compared to the control treatment against *S. aureus* ATCC 25923 (D) and *P. aeruginosa* ATCC 27853 (E).

contrast, both pNiHyPH and pNiMaMH maintained and even increased their inhibition zones over time, with pNiMaMH showing slightly better performance against *S. aureus* due to its faster release of MP-L [I5R8]. While the single-dose treatment loses its efficacy after 8 h, both DRPHs

show prolonged inhibition. Interestingly, the pNiHyPH displays a continuous rise in the inhibitory zone over time, demonstrating its slower release profile and prolonged antibacterial efficacy against *P. aeruginosa* (see Fig. 10C). The quantitative measures of bacterial

growth for *S. aureus* and *P. aeruginosa* are displayed in Fig. 10D and 10E, respectively. A better view of the antibacterial effectiveness over time is given by these graphics. In both bacterial strains, the single-dose injection of MP-L [I5R8] initially reduces bacterial growth, but after 8 h bacterial growth recovery is observed when the peptide concentration drops. In contrast, both DRPHs with sustained release of MP-L [I5R8] achieve prolonged antibacterial activity. Bacterial growth remains suppressed for extended periods (up to 168 h) in both bacterial strains, demonstrating the continuous release of the MP-L [I5R8]. For *S. aureus*

(Fig. 11D), the pNiMaMH shows a slightly better inhibition effect, correlating with its faster release profile. This is to be expected because *P. aeruginosa* has a lower MIC than *S. aureus*, and pNiMaMH delivers MP-L [I5R8] more quickly to achieve this inhibition. The pNiHyPH works better and has a longer-lasting antibacterial impact against *P. aeruginosa* (Fig. 10E). The slower release of MP-L [I5R8] from pNiHyPH allows for a longer extended effect, which is critical in managing bacteria with higher resistance. This correlates to the higher time-kill value for *P. aeruginosa*. The results from Fig. 10 emphasize the

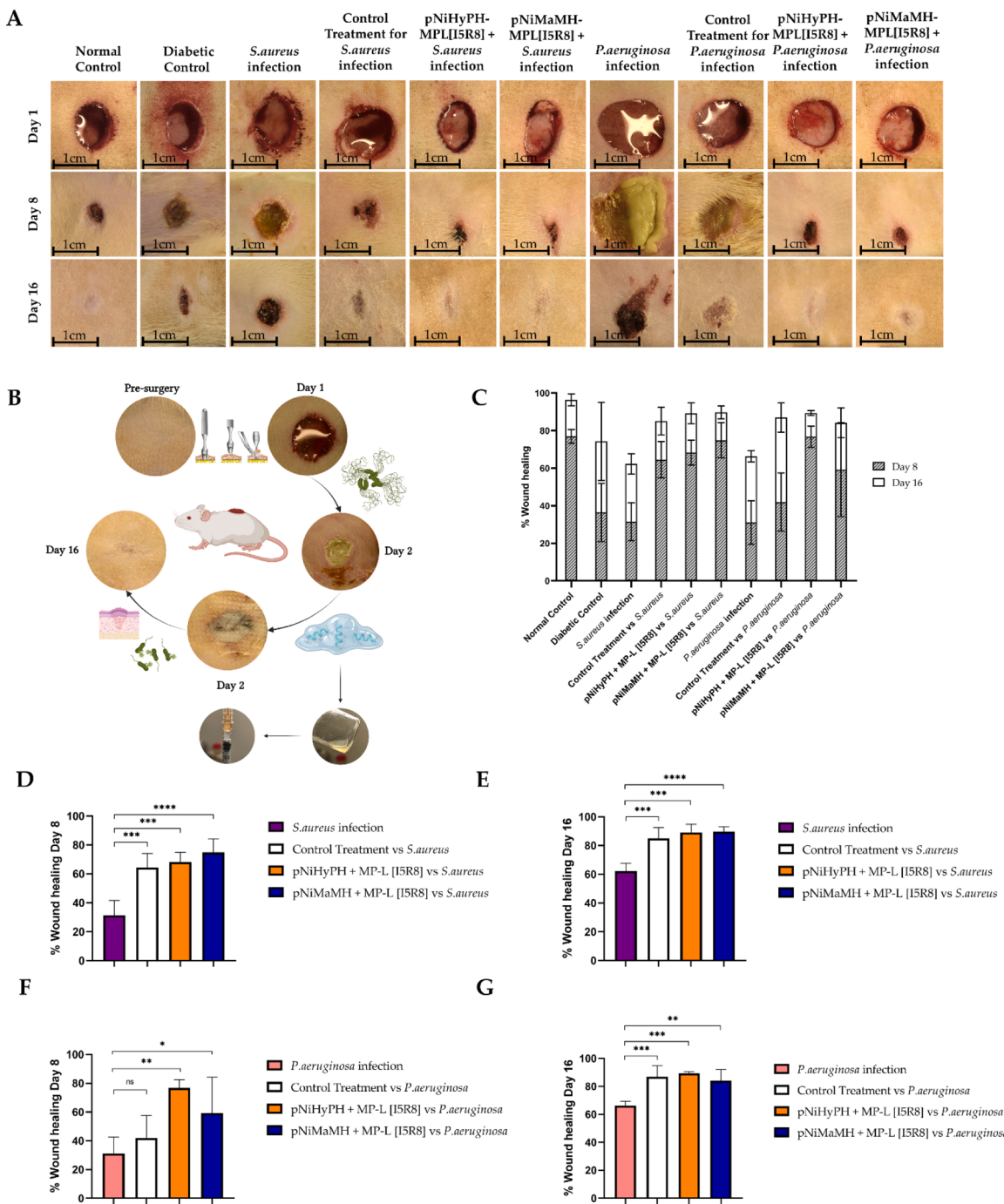


**Fig. 11.** *In vivo* antibacterial activity of MP-L [I5R8]-loaded DRPHs in a diabetic SD rat model. The evolution of the wounds in each group is shown on days 1, 8, and 16 (A). Summary diagram of the methodology used for wound generation, infection, treatment with MP-L [I5R8]-loaded DRPHs, and follow-up (B). General assay results for each group concerning wound healing on days 8 and 16 (C). Comparison between the results of recovery of infected wounds for the untreated group, with control treatment, with MP-L [I5R8]-loaded pNiHyPH and MP-L [I5R8]-loaded pNiMaMH against *S. aureus* ATCC 25923 on days 8 (D) and 16 (E), and against *P. aeruginosa* ATCC 27853 on days 8 (F) and 16 (G) respectively. Statistical analysis of the wound closure process was performed using one-way ANOVA with statistically significant *p* values < 0.05 \*; *p* < 0.01 \*\*; *p* < 0.001 \*\*\*; and *p* < 0.0001 \*\*\*\*.

advantages of using pNiHyPH and pNiMaMH for the sustained release of the antimicrobial peptide MP-L [I5R8]. Both DRPHs successfully provide a prolonged antibacterial effect, which outperforms a single-dose administration by maintaining bacterial growth suppression for up to 168 h. Because the pNiMaMH releases the MP-L [I5R8] more quickly, and it exhibits superior early inhibition against the more potent *S. aureus*. The slower release profile of pNiHyPH, however, has a longer-lasting antibacterial activity, especially against *P. aeruginosa*, which has a greater time-kill value. These findings show that the choice between pNiHyPH and pNiMaMH could be modified depending on the target bacteria and the clinical necessity. A slower-releasing system, such as pNiHyPH may offer superior long-term control for *P. aeruginosa* infections, whereas a faster-releasing system, such as pNiMaMH, may be more successful for *S. aureus* infections.

### 3.6. In vivo antibacterial activity of MP-L—loaded DRPHs

The effectiveness of MP-L [I5R8]-loaded pNiHyPH and MPL-loaded pNiMaMH, in improving wound healing in diabetic mice infected with *S. aureus* and *P. aeruginosa* was evaluated. The findings based on the visual progression of wound healing and quantitative data analysis demonstrate the significant therapeutic potential of these treatments in accelerating wound closure in infected diabetic wounds. Fig. 11A illustrates how wound healing progressed over 16 days in three separate conditions: control, infection, and treatment groups. Wounds in healthy, non-diabetic mice healed as predicted in the Normal Control Group (Non-Diabetic, No Infection). By Day 16, wounds were fully closed, indicating a normal wound-healing process in the absence of infection or diabetes. Concerning the Diabetic Control Group (No Infection, Untreated), the diabetic control group's wounds showed poor healing. In comparison to the typical control, wounds showed little healing by Day 8 and continued to remain considerably open by Day 16. This demonstrates how diabetic diseases are known for their delayed wound healing. In the untreated *S. aureus*-infected group, the wounds showed considerable delays in healing. By Day 8, there was noticeable enlargement of wounds with signs of inflammation and necrosis. Even though healing had advanced by Day 16, the wounds had not completely healed. Larger wounds, more intense inflammation, and the development of yellowish exudates were indicative of more severe wound damage in the untreated *P. aeruginosa*-infected group than in the *S. aureus*-infected group. Healing was notably slower and by Day 16, the wounds remained significantly open. In the treated groups with MP-L [I5R8]-loaded pNiHyPH and MP-L [I5R8]-loaded pNiMaMH, for both *S. aureus* and *P. aeruginosa* infections the treatment groups demonstrated marked improvements in wound healing. In comparison to the untreated controls, the wounds in the treated groups were much smaller and less inflammatory by Day 8. On Day 16, treatment wounds showed significant improvement (*P. aeruginosa* groups) or were almost closed (*S. aureus* groups). The improved healing rates in treated wounds as opposed to untreated ones are demonstrated by the visible progression.

Fig. 11B illustrates the experimental design after diabetes was induced in the specimens. On day 1, a wound was created at the suprascapular level and infected with the bacterial strains under study. Twenty-four hours after bacterial inoculation, either the control treatment or MP-L [I5R8]-loaded hydrogels were applied as appropriate. Wound progression was then monitored up to day 16. The quantitative data of wound healing in Fig. 11C illustrates the percentage of wound healing on Days 8 and 16 across all experimental groups. By Day 16, the usual control group showed almost 100% wound healing, as was to be expected. On the other hand, the diabetic control group demonstrated a wound healing rate of only 20% by Day 8 and around 50% by Day 16, which is indicative of the compromised healing process linked to diabetes. Less than 30% of the *S. aureus*-infected group recovered by Day 8 and about 50% by Day 16, indicating delayed healing. This demonstrates how an *S. aureus* infection hinders the healing of wounds. Conversely, the group infected with *P. aeruginosa* but not treated showed much worse wound

healing, with less than 20% healing by Day 8 and only about 40% healing by Day 16. This illustrates how dangerous and difficult *P. aeruginosa* infections are in diabetic wounds. Both MP-L [I5R8]-loaded DRPHs treatments markedly accelerated wound healing in the *S. aureus*-infected groups. Treatment groups showed 60–70% repair by Day 8, and nearly 90% healing by Day 16. The *P. aeruginosa*-infected groups recovered more slowly than the treated groups, although they still did better than the untreated controls. Healing rates were 45–60% by Day 8, and both treatments reached about 80% healing by Day 16. Even though treating wounds infected with *P. aeruginosa* was more difficult, both formulations offered a substantial therapeutic benefit. Fig. 11D-G show statistical comparisons of wound healing between the untreated and treated groups on Days 8 and 16 highlighting the efficacy of the treatments. As of Day 8, only around 30% of the *S. aureus* infection group that received no treatment had healed (Fig. 11D). By this time point, 60–70% of the wounds in both treatment groups (MP-L [I5R8]-loaded pNiHyPH and MP-L [I5R8]-loaded pNiMaMH) had healed ( $p < 0.0001$ ). By Day 16, the treated groups showed nearly 90% wound closure, while the untreated group only reached ~50% healing (Fig. 11E). Both treatments were effective in encouraging wound closure, as evidenced by the highly substantial ( $p < 0.0001$ ) differences between the treated and untreated groups. By Day 8, less than 20% of the wounds in the untreated *P. aeruginosa* group (Fig. 11F) had healed. Significantly greater healing rates (45–60%) were attained by the therapy groups, and the differences were statistically significant ( $p < 0.01$ ). By Day 16 (see Fig. 11G), the untreated *P. aeruginosa* group had only achieved about 40% healing, while both treated groups reached around 80%. The differences between the treated and untreated groups were again significant ( $p < 0.01$ ), confirming the efficacy of both treatments in promoting wound healing, even in more severe infections. The wound healing in the diabetic control group was severely impaired, with significantly delayed closure compared to the normal control group. This finding is in line with the known fact that diabetes inhibits the healing of wounds. Infections with *P. aeruginosa* and *S. aureus* both made diabetic mice's poor wound healing worse. Comparing the untreated infected groups to the diabetic control group without infection, the untreated infected groups had noticeably slower closure rates and bigger wounds. Compared to *S. aureus*, the severity of *P. aeruginosa* infections caused considerably more delayed recovery. The use of MP-L [I5R8]-loaded pNiHyPH and MP-L [I5R8]-loaded pNiMaMH treatments markedly improved wound healing in diabetic mice infected with *P. aeruginosa* and *S. aureus*. By Day 16, wound closure in the treated groups was substantially higher compared to untreated controls, with nearly complete closure in the *S. aureus* treated groups and significant improvement in the *P. aeruginosa* groups. Although both treatments were effective in promoting wound healing in *P. aeruginosa*-infected wounds, healing was generally slower compared to *S. aureus* infections. This data reveals the greater virulence and difficulty in treating *P. aeruginosa*, a pathogen that is notorious for its resistance to many treatments [73].

A typical commercial product was utilized as the control treatment in this trial, and it was once applied daily for 16 days (Topical 2% mupirocin for the treatment of *S. aureus* and 1% silver sulfadiazine ointment for the treatment of *P. aeruginosa*) at the recommended dosage. On the other hand, the MP-L [I5R8]-loaded pNiMaMH and pNiHyPH treatments were only administered once (on Day 2). Both MP-L [I5R8]-loaded DRPH therapies showed notable increases in wound healing with only one application; indeed, they performed better than the commercial treatment, which needed to be administered every day. This demonstrates the MP-L [I5R8] formulations' better and long-lasting efficacy since they outperformed the daily-applied commercial medication in terms of wound closure after just one application.

To analyze wound closure in the *in vivo* assay, a one-way ANOVA was performed to compare treatment groups with the control. Four independent analyses were conducted: (1) comparing the *S. aureus* infection group with the control treatment and the application of MP-L[I5R8]-

loaded pNiHyPH and MP-L[I5R8]-loaded pNiMaMH on days 8 and 16, respectively; and (2) comparing the *P. aeruginosa* infection group with the control treatment and the same MP-L[I5R8]-loaded DRPH treatments on days 8 and 16, respectively. A p-value < 0.05 was considered statistically significant.

**Fig. 11D:** The control treatment with mupirocin and the application of MP-L[I5R8]-loaded pNiHyPH on day 8 showed a p-value < 0.001 when comparing the wound closure area to *S. aureus* infection without treatment. MP-L[I5R8]-loaded pNiMaMH exhibited an even higher statistical significance (p-value < 0.0001). These statistical differences remained significant for each group on day 16 (**Fig. 11E**). However, no statistically significant differences were observed between the treatment groups for *S. aureus* infection.

**Fig. 11F:** For the control treatment with silver sulfadiazine, no statistically significant differences were found when comparing wound closure areas to *P. aeruginosa* infection without treatment on day 8. However, the application of MP-L[I5R8]-loaded pNiMaMH and MP-L[I5R8]-loaded pNiHyPH resulted in p-values of < 0.05 and < 0.01, respectively, on day 8. By day 16, an improvement was observed in the control treatment, as reflected by a statistically significant difference compared to the infection without treatment (p-value < 0.001), MP-L[I5R8]-loaded pNiMaMH (p-value < 0.01), and MP-L[I5R8]-loaded pNiHyPH (p-value < 0.001) (**Fig. 11G**).

These findings indicate that MP-L[I5R8]-loaded pNiHyPH and MP-L[I5R8]-loaded pNiMaMH are useful therapies for improving wound healing in diabetic mice harboring *S. aureus* and *P. aeruginosa* infections. Even in the presence of infection the therapies greatly speed up wound closure. For instance, by Day 16 the *S. aureus* treated groups had almost fully healed. Even though *P. aeruginosa* infections were more difficult, both therapies significantly enhanced recovery as compared to the untreated groups. In addition to visual monitoring of the wounds, temperature variation was monitored for each specimen in the study on day 1 (wound generation and bacterial inoculation if applicable), day 2 (treatment application as appropriate), and days 8 and 16, the graphs are shown in **Figure S7**. For all groups, an increase in temperature was evident in the wound area on day 2, attributable to the inflammatory process caused by surgery and bacterial inoculation. As shown in A, in untreated infected diabetic rats, there was an increase in temperature that was sustained until day 16 compared to the uninfected groups. In B, the monitoring of temperature variation is compared for the groups infected with *S. aureus*, where a recovery of basal temperature is shown for the control treatment groups and with DRPHs loaded with MP-L[I5R8], where the pNiMaMH loaded with MP-L[I5R8] shows a faster decrease in temperature. On the other hand, in the case of infection caused by *P. aeruginosa*, the treatment that showed a faster decrease in temperature was the pNiHyPH loaded with MP-L[I5R8], shown in C.

Regarding the degradation of DRPHs in the *in vivo* assay, studies on the degradation of pNIPAM-based hydrogels have been reported in the literature [74 - 76]. These studies indicate that, in copolymerized systems, degradation occurs over a period of 10–20 days when an acidic component (e.g., acrylic acid, lactic acid) is incorporated into the polymeric network [74,75]. In the case of pNiHyPH, hydromuconic acid has been incorporated, while in pNiMaMH, maleic acid has been used. The degradation of DRPHs is expected to begin with the hydrolysis of these acidic comonomers when subjected to a constant temperature near the LCST (32–37°C) [75]. This aligns with observations from our *in vivo* assay, where, from day 8 onwards, some specimens exhibited a noticeable absence of DRPHs, accompanied by advanced wound healing and a lack of infection. These findings support the potential of pNiHyPH and pNiMaMH for topical applications.

These results suggest that these formulations may prove to be efficacious therapeutic alternatives for the management of diabetic patients' chronic wounds, especially those exacerbated by bacterial infections.

### 3.7. Histological analysis

The histological analyses are shown in **Fig. 12**. Hematoxylin-Eosin (H&E), Masson's Trichrome, and Picosirius Red stains were employed. H&E staining enabled the assessment of the overall tissue structure, while Masson's Trichrome highlighted collagen distribution and organization. Additionally, Picosirius Red, observed under polarized light, facilitated the evaluation of collagen fiber maturity and orientation in both treated and untreated groups.

The untreated infected groups, Group 3 (*S. aureus*) and Group 4 (*P. aeruginosa*) demonstrated incomplete wound healing and disorganized collagen structures. H&E staining revealed a moderate inflammatory cell infiltration, while Masson's Trichrome staining showed irregular collagen deposition. Picosirius Red staining revealed an irregular distribution of type I and type III collagen, with reduced collagen type I levels, suggesting an unstable tissue structure and delayed maturation process in these groups.

Moderate improvements were observed in the antibiotic-treated groups, Group 5 (*S. aureus* with mupirocin) and Group 6 (*P. aeruginosa* with silver sulfadiazine). Masson's trichrome revealed some collagen alignment in Group 6, while H&E staining showed a reduction in inflammatory cells in both groups. Picosirius red staining showed a slight increase in collagen type I content compared to the untreated groups. These findings suggest enhanced structural repair, though still in progress.

The MP-L[I5R8]-loaded DRPH-treated groups exhibited significant advances in wound healing. Groups 7 and 8 (*S. aureus* treated with MP-L[I5R8]-loaded pNiHyPH and MP-L-loaded pNiMaMH) and Groups 9 and 10 (*P. aeruginosa* treated with MP-L[I5R8]-loaded pNiHyPH and MP-L[I5R8]-loaded pNiMaMH) showed a marked reduction in inflammatory cell infiltration, as seen in H&E staining, and more organized collagen patterns in Masson's Trichrome staining. Picosirius Red staining showed substantial increases in both collagen I and III, particularly in MP-L[I5R8]-loaded pNiMaMH-treated groups (Groups 8 and 10), indicating a more mature and stable tissue structure. Group 10, in particular, showed the highest collagen type I content, closely resembling the healthy tissue structure observed in the Normal Control (NC).

The control groups, stained with H&E, Masson's Trichrome, and Picosirius Red, provided a baseline. Group 1 (NC) showed a well-organized epidermis, minimal inflammatory cells, and a stable balance of collagen types I and III under Picosirius Red staining. These findings suggest an environment that maintains skin elasticity and functionality, promoting scar integration with surrounding tissue without compromising strength. In contrast, Group 2 (Diabetic Control) exhibited slower healing, with persistent inflammation and lower collagen I content, indicative of an early healing phase or incomplete tissue repair, highlighting the impaired structural integrity typical of diabetic tissue.

In conclusion, the staining techniques revealed that hydrogel treatments, particularly MP-L[I5R8]-loaded pNiMaMH, promoted highly organized and mature collagen deposition, accompanied by a significant reduction in inflammatory cell infiltration, approaching the characteristics of healthy, non-infected tissue. The high levels of collagen types I and III in Picosirius Red staining for MP-L[I5R8]-loaded pNiMaMH-treated groups indicate a mature, stable, and efficient wound-healing process. This suggests that MP-L[I5R8]-loaded pNiMaMH may offer therapeutic advantages over antibiotics by creating an environment that promotes organized collagen synthesis and deposition and effective tissue recovery in infected wounds.

## 4. Conclusions

The development and comprehensive analysis of the DRPHs such as pNiHyPH and pNiMaMH represent a substantial advancement in the field of localized and sustained drug delivery, specifically for the treatment of chronic wounds infected with multidrug-resistant bacteria.

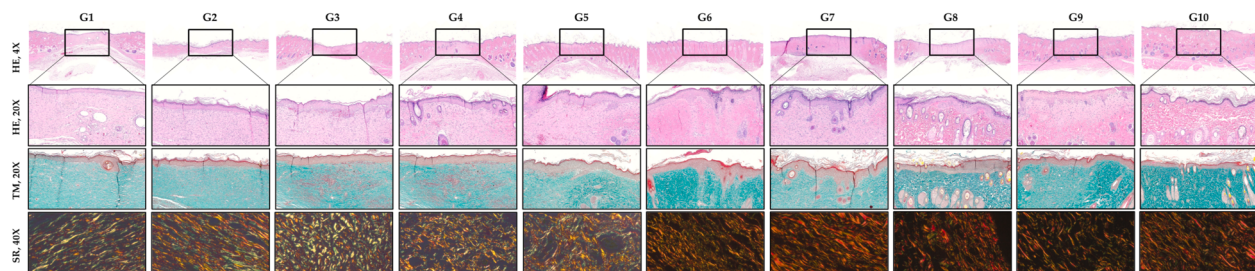


**Fig. 12.** Histological sections of healing skin from 10 experimental groups (G1-G10), were stained with Hematoxylin-Eosin (HE), Masson's Trichrome (TM), and Sirius Red (SR) to assess tissue structure and collagen organization. Staining was performed at different magnifications: HE at 4x and 20x, TM at 20x, and SR at 40x under polarized light. The HE stains provide an overview of the general morphology and organization of the epidermal and dermal layers. Masson's Trichrome highlights collagen within the connective tissue, emphasizing its distribution and density in the dermis. SR staining, observed under polarized light, enables precise characterization of collagen fibers, with type I collagen appearing in red tones and type III collagen in green tones, demonstrating changes in extracellular matrix organization and remodeling during the healing process.

These DRPHs, based on NIPAM with carboxylic acid co-monomers (Hy and Ma, respectively), exhibit the ability to transition from liquid to gel at physiological temperature, allowing injectable application and *in situ* gelation at the infection site. This thermoresponsive behavior ensures a controlled release of the incorporated antimicrobial peptide MP-L [I5R8], ideal for treating infections in complex wound environments, such as diabetic foot ulcers.

The successful synthesis of both DRPHs was confirmed via FTIR and <sup>1</sup>H NMR, which indicated the effective copolymerization of NIPAM with Hy and Ma, essential for creating electrostatic interactions with positively charged peptides like MP-L [I5R8]. Thermal stability, determined through TGA and DTG, revealed robustness up to approximately 400 °C, underscoring the HGs' suitability for biomedical applications. The swelling behavior of each DRPH provided distinct advantages: pNiHyPH displayed a controlled swelling of 509 %, offering a steady release suitable for prolonged treatments, while pNiMaMH showed an enhanced swelling capacity of 1596 %, enabling a faster initial release of the antimicrobial agent. The rheological analysis further demonstrated that both HGs transition from a liquid to a gel state at body temperature, with pNiHyPH showing a more elastic, stable network suitable for maintaining structural integrity over time.

The DRPHs demonstrated excellent biocompatibility in NIH-3T3 fibroblast cultures, with MP-L [I5R8] showing minimal hemolytic activity and high cell viability in the same fibroblast line, confirming their suitability for biomedical applications. *In vitro*, antimicrobial tests confirmed their sustained efficacy against *S. aureus* and *P. aeruginosa*, two of the most problematic MDR bacterial strains associated with wound infections. *In vivo* studies in diabetic rats further demonstrated the therapeutic benefits of these DRPHs, as they promoted rapid wound closure, reduced infection, significantly decreased inflammatory cell infiltration, and supported tissue healing, evidenced by organized collagen deposition and a mature tissue structure closely resembling healthy skin.

The release kinetics of MP-L [I5R8] from both DRPHs followed a dual-phase profile, with pNiMaMH facilitating faster release in the early phase (42.86 % release) and pNiHyPH showing a more controlled release profile ideal for extended therapy. Over 168 h, pNiMaMH reached a cumulative release of approximately 70 %, while pNiHyPH achieved 60 %. Kinetic modeling, particularly with the Korsmeyer-Peppas model, indicated a non-Fickian mechanism involving both diffusion and matrix relaxation, highlighting the ability of the DRPHs to deliver a controlled, prolonged release of the AMP.

In summary, our study presents the development and characterization of DRPHs incorporating NIPAM-based copolymers for localized and sustained AMP release. Compared to conventional NIPAM hydrogels, our DRPHs exhibit dual pH- and temperature-responsiveness, enabling controlled release kinetics and enhanced peptide retention. The *in vivo* wound healing model demonstrated effective infection clearance and

tissue regeneration, highlighting the potential of these hydrogels for advanced wound care applications. While DRPHs offer advantages such as injectability, biocompatibility, and tunable drug release, further optimization of mechanical stability and drug compatibility could expand their biomedical applications. These findings contribute to the growing field of stimuli-responsive biomaterials and provide a foundation for future translational research in drug delivery and wound healing therapies.

These findings underline the versatility and clinical potential of pNiHyPH and pNiMaMH in infection management and wound care. pNiHyPH, with its controlled release and stable network, is ideal for applications requiring long-term therapy, while pNiMaMH's rapid swelling and release profile is beneficial for situations needing immediate therapeutic action followed by sustained drug delivery. The unique dual-stimuli responsiveness and strong antimicrobial efficacy of these hydrogels position them as promising candidates for next-generation biomaterials in regenerative medicine and infection control.

In conclusion, the dual-stimuli-responsive hydrogels pNiHyPH and pNiMaMH offer a novel, adaptable approach to treat complex infections in chronic wounds. By providing a rapid initial response coupled with sustained therapeutic effects, these DRPHs present an innovative solution for managing infections and promoting wound healing, paving the way for further developments in targeted, injectable drug delivery systems for various clinical applications.

#### Declaration of Generative AI and AI-assisted technologies in the writing process

During the preparation of this work, the authors used ChatGPT to improve the grammar, clarity, and overall readability of article. After using this tool, the authors reviewed and edited the content as needed and takes full responsibility.

#### CRediT authorship contribution statement

**Fernanda Andrade:** Methodology, Investigation. **Sekar Vijayakumar:** Validation, Methodology. **Rodrigo Moore-Carrasco:** Visualization, Validation, Conceptualization. **Gustavo Cabrera-Barjas:** Investigation, Formal analysis. **Paulo Salinas:** Investigation, Formal analysis, Data curation. **Esteban F. Durán-Lara:** Writing – original draft, Visualization, Validation, Supervision, Project administration, Methodology, Investigation, Funding acquisition, Formal analysis, Data curation, Conceptualization. **Juan Lara:** Visualization, Formal analysis. **Marcelo Guerrero:** Writing – original draft, Methodology, Investigation, Conceptualization. **Diana Rafael:** Methodology, Investigation. **Adolfo Marican:** Methodology, Investigation.

## Declaration of Competing Interest

The authors declare that they have no known competing financial interests or personal relationships that could have appeared to influence the work reported in this paper.

## Acknowledgements

This work was supported by ANID FONDECYT REGULAR (Chile) through Project N° 1210476, ANID-FONDEQUIP EQM230060 (Chile), and ANID-FOVI (Chile) through Project N° 230019 from Prof. Esteban F. Durán- Lara.

## Appendix A. Supporting information

Supplementary data associated with this article can be found in the online version at [doi:10.1016/j.colsurfb.2025.114636](https://doi.org/10.1016/j.colsurfb.2025.114636).

## Data availability

No data was used for the research described in the article.

## References

- [1] J. O'Neill, Antimicrobial resistance: tackling a crisis for the health and wealth of nations, *Rev. Antimicrob. Resist.* (December) (2016).
- [2] A.K. Murray, The novel coronavirus COVID-19 outbreak: global implications for antimicrobial resistance, *Front. Microbiol.* 11 (2020), <https://doi.org/10.3389/fmicb.2020.01020>.
- [3] J. Hsu, 2020, How covid-19 is accelerating the threat of antimicrobial resistance' [10.1136/bmj.m1983](https://doi.org/10.1136/bmj.m1983).
- [4] C.A. Arias, B.E. Murray, Antibiotic-resistant bugs in the 21st century — a clinical super-challenge, *N. Engl. J. Med.* 360 (5) (2009), <https://doi.org/10.1056/nejmop0804651>.
- [5] S.S. Kadri, Key Takeaways from the U.S. CDC's 2019 Antibiotic Resistance Threats Report for Frontline Providers (2020), <https://doi.org/10.1097/CCM.00000000000004371>.
- [6] M.-L. Shi, X.-R. Quan, L.-M. Tan, H.-L. Zhang, A.-Q. Yang, Identification and antibiotic susceptibility of microorganisms isolated from diabetic foot ulcers: a pathological aspect, *Exp. Ther. Med.* 25 (1) (2022), <https://doi.org/10.3892/etm.2022.11752>.
- [7] J.M. Sweere, et al., The immune response to chronic *Pseudomonas aeruginosa* wound infection in immunocompetent mice, *Adv. Wound Care (New Rochelle)* 9 (2) (2020), <https://doi.org/10.1089/wound.2019.1039>.
- [8] C. Dunyach-Remy, C.N. Essebe, A. Sotto, J.P. Lavigne, *Staphylococcus aureus* toxins and diabetic foot ulcers: Role in pathogenesis and interest in diagnosis (2016), <https://doi.org/10.3390/toxins8070209>.
- [9] A. Pitiot, et al., Mucosal administration of anti-bacterial antibodies provide long-term cross-protection against *Pseudomonas aeruginosa* respiratory infection, *Mucosal Immunol.* 16 (3) (2023), <https://doi.org/10.1016/j.mucimm.2023.03.005>.
- [10] D. Lahiri, M. Nag, A. Dey, T. Sarkar, S. Pati, R.R. Ray, Nanoparticles based antibacterial vaccines: Novel strategy to combat antimicrobial resistance, *Process Biochem.* 119 (2022), <https://doi.org/10.1016/j.procbio.2022.05.011>.
- [11] Y. Zhu, et al., The design of cell-selective tryptophan and arginine-rich antimicrobial peptides by introducing hydrophilic uncharged residues, *Acta Biomater.* 153 (2022), <https://doi.org/10.1016/j.actbio.2022.09.028>.
- [12] G. Cheng, M. Dai, S. Ahmed, H. Hao, X. Wang, Z. Yuan, Antimicrobial drugs in fighting against antimicrobial resistance (2016), <https://doi.org/10.3389/fmicb.2016.00470>.
- [13] J. Mwangi, et al., The antimicrobial peptide ZY4 combats multidrugresistant *Pseudomonas aeruginosa* and *Acinetobacter baumannii* infection, *Proc. Natl. Acad. Sci. USA* 116 (52) (2019), <https://doi.org/10.1073/pnas.1909585117>.
- [14] P. Bhadra, J. Yan, J. Li, S. Fong, S.W.I. Siu, AmPEP: sequence-based prediction of antimicrobial peptides using distribution patterns of amino acid properties and random forest, *Sci. Rep.* 8 (1) (2018), <https://doi.org/10.1038/s41598-018-19752-w>.
- [15] M. Karapetian, et al., Evaluation of the synergistic potential and mechanisms of action for de novo designed cationic antimicrobial peptides, *Heliyon* 10 (6) (2024), <https://doi.org/10.1016/j.heliyon.2024.e27852>.
- [16] K. Browne, et al., A new era of antibiotics: The clinical potential of antimicrobial peptides (2020), <https://doi.org/10.3390/ijms21197047>.
- [17] H. Cohen, et al., Interaction of pexiganan (MSI-78)-derived analogues reduces inflammation and TLR4-mediated cytokine secretion: a comparative study, *ACS Omega* 8 (20) (2023), <https://doi.org/10.1021/acsomega.3c00850>.
- [18] A. Pfalzgraff, K. Brandenburg, G. Weindl, Antimicrobial peptides and their therapeutic potential for bacterial skin infections and wounds (2018), <https://doi.org/10.3389/fphar.2018.00281>.
- [19] A. Hanafiah, S.N.A. Abd Aziz, Z.N. Md Nesran, X.C. Wezen, M.F. Ahmad, Molecular investigation of antimicrobial peptides against *Helicobacter pylori* proteins using a peptide-protein docking approach, *Heliyon* 10 (6) (2024), <https://doi.org/10.1016/j.heliyon.2024.e28128>.
- [20] L.N. Irazazabal, et al., Selective amino acid substitution reduces cytotoxicity of the antimicrobial peptide mastoparan, *Biochim. Biophys. Acta Biomembr.* 1858 (11) (2016), <https://doi.org/10.1016/j.bbamem.2016.07.001>.
- [21] A. Savitskaya, J. Masso-Silva, I. Haddaoui, S. Enany, Exploring the arsenal of antimicrobial peptides: Mechanisms, diversity, and applications (2023), <https://doi.org/10.1016/j.biochi.2023.07.016>.
- [22] B. Lin, et al., Systematic comparison of activity and mechanism of antimicrobial peptides against nosocomial pathogens, *Eur. J. Med. Chem.* 231 (2022), <https://doi.org/10.1016/j.ejmech.2022.114135>.
- [23] A. Pereira, et al., Rational design of hydrogels for cationic antimicrobial peptide delivery: a molecular modeling approach, *Pharmaceutics* 15 (2) (2023), <https://doi.org/10.3390/pharmaceutics15020474>.
- [24] M. Guerrero, et al., Hydrogel-antimicrobial peptide association: a novel and promising strategy to combat resistant infections, *Colloids Surf. B Biointerfaces* 247 (2025) 114451, <https://doi.org/10.1016/j.colsurfb.2024.114451>.
- [25] P. Kumar, J.N. Kizhakkedathu, S.K. Straus, Antimicrobial peptides: diversity, mechanism of action and strategies to improve the activity and biocompatibility in vivo (2018), <https://doi.org/10.3390/biom8010004>.
- [26] V. Pertici, et al., Degradable and injectable hydrogel for drug delivery in soft tissues, *Biomacromolecules* 20 (1) (2019), <https://doi.org/10.1021/acs.biomac.8b01242>.
- [27] F. Ávila-Salas, E.F. Durán-Lara, An overview of injectable thermo-responsive hydrogels and advances in their biomedical applications, *Curr. Med. Chem.* 27 (34) (2019), <https://doi.org/10.2174/092986732566190603110045>.
- [28] X. Gao, et al., pH- and thermo-responsive poly(N-isopropylacrylamide-co-acrylic acid derivative) copolymers and hydrogels with LCST dependent on pH and alkyl side groups, *J. Mater. Chem. B* 1 (41) (2013), <https://doi.org/10.1039/c3tb20901f>.
- [29] C. Liu, Q. Zhang, S. Zhu, H. Liu, J. Chen, Preparation and applications of peptide-based injectable hydrogels (2019), <https://doi.org/10.1039/c9ra05934b>.
- [30] F. Joubert, P.C.P. Denn, Y. Guo, G. Pasparakis, Comparison of thermoresponsive hydrogels synthesized by conventional free radical and RAFT polymerization, *Materials* 12 (7) (2019), <https://doi.org/10.3390/ma12172697>.
- [31] M. Cao, et al., Reversible thermoresponsive peptide-PNIPAM hydrogels for controlled drug delivery, *Biomacromolecules* 20 (9) (2019), <https://doi.org/10.1021/acs.biomac.9b01009>.
- [32] M.A. Haq, Y. Su, D. Wang, Mechanical properties of PNIPAM based hydrogels: a review (2017), <https://doi.org/10.1016/j.mssec.2016.09.081>.
- [33] X. Wang, C.-X. Yuan, B. Xu, Z. Yu, Diabetic foot ulcers: Classification, risk factors and management, *World J. Diabetes* 13 (12) (2022), <https://doi.org/10.4239/wjd.v13.i12.1049>.
- [34] J.H. Lee, Injectable hydrogels delivering therapeutic agents for disease treatment and tissue engineering (2018), <https://doi.org/10.1186/s40824-018-0138-6>.
- [35] V. Gounden, M. Singh, Hydrogels and Wound Healing: Current and Future Prospects (2024), <https://doi.org/10.3390/gels10010043>.
- [36] R. Gu, et al., Research progress related to thermosensitive hydrogel dressings in wound healing: a review (2023), <https://doi.org/10.1039/d3na00407d>.
- [37] S. Lanzalaco, E. Armelin, Poly(N-isopropylacrylamide) and copolymers: A review on recent progresses in biomedical applications (2017), <https://doi.org/10.3390/gels10040036>.
- [38] H. Chen, et al., An injectable self-healing coordinative hydrogel with antibacterial and angiogenic properties for diabetic skin wound repair, *NPG Asia Mater.* 11 (1) (2019), <https://doi.org/10.1038/s41427-018-0103-9>.
- [39] N. Higashi, S. Matsubara, S.N. Nishimura, T. Koga, Stepwise thermo-responsive amino acid-derived triblock vinyl polymers: ATRP synthesis of polymers, aggregation, and gelation properties via flower-like micelle formation, *Materials* 11 (3) (2018), <https://doi.org/10.3390/ma11030424>.
- [40] R. Jalababu, S. Satyavati Veni, K.V.N.S. Reddy, Development, characterization, swelling, and network parameters of amino acid grafted guar gum based pH responsive polymeric hydrogels, *Int. J. Polym. Anal. Charact.* 24 (4) (2019), <https://doi.org/10.1080/1023666X.2019.1594058>.
- [41] O. Forero-Doria, et al., Supramolecular hydrogels based on cellulose for sustained release of therapeutic substances with antimicrobial and wound healing properties, *Carbohydr. Polym.* 242 (2020), <https://doi.org/10.1016/j.carbpol.2020.116383>.
- [42] F. Ávila-Salas, et al., Film dressings based on hydrogels: simultaneous and sustained-release of bioactive compounds with wound healing properties, *Pharmaceutics* 11 (9) (2019), <https://doi.org/10.3390/pharmaceutics11090447>.
- [43] S.A.S. Tabassi, F.S.M. Tekie, F. Hadizadeh, R. Rashid, E. Khodaverdi, S.A. Mohajeri, Sustained release drug delivery using supramolecular hydrogels of the triblock copolymer PCL-PEG-PCL and  $\alpha$ -cyclodextrin, *J. Solgel Sci. Technol.* 69 (1) (2014), <https://doi.org/10.1007/s10971-013-3200-9>.
- [44] G. Carreño, et al., Development of “on-demand” thermo-responsive hydrogels for anti-cancer drugs sustained release: Rational design, in silico prediction and in vitro validation in colon cancer models, *Mater. Sci. Eng. C* 131 (2021), <https://doi.org/10.1016/j.mscc.2021.112483>.
- [45] I.P. Saébo, M. Björås, H. Franzén, E. Helgesen, J.A. Booth, Optimization of the hemolysis assay for the assessment of cytotoxicity, *Int. J. Mol. Sci.* 24 (3) (2023), <https://doi.org/10.3390/ijms24032914>.
- [46] P. Pintor, P. Ratnibin, N. Tassaneesuwan, R. Chiangnoon, P. Uttayarat, Cytotoxicity evaluation of hydrogel sheet dressings fabricated by gamma irradiation: extract and semi-direct contact tests, *Trends Sci.* 19 (13) (2022), <https://doi.org/10.48048/tis.2022.4583>.

- [47] J. Trudel, S.P. Massia, Assessment of the cytotoxicity of photocrosslinked dextran and hyaluronan-based hydrogels to vascular smooth muscle cells, *Biomaterials* 23 (16) (2002), [https://doi.org/10.1016/S0142-9612\(02\)00009-1](https://doi.org/10.1016/S0142-9612(02)00009-1).
- [48] M.O. Wang, J.M. Etheridge, J.A. Thompson, C.E. Vorwald, D. Dean, J.P. Fisher, Evaluation of the in vitro cytotoxicity of cross-linked biomaterials, *Biomacromolecules* 14 (5) (2013), <https://doi.org/10.1021/bm301962f>.
- [49] CLSI, , 2023M100-ED33: Performance Standards for Antimicrobial Susceptibility Testing2023CLSI M100-ED33: Performance Standards for Antimicrobial Susceptibility Testing33rd Edition2023.
- [50] S.M. Daly, C.R. Sturge, D.E. Greenberg, Inhibition of bacterial growth by peptide-conjugated morpholino oligomers, *Methods Mol. Biol.* 1565 (2017), [https://doi.org/10.1007/978-1-4939-6817-6\\_10](https://doi.org/10.1007/978-1-4939-6817-6_10).
- [51] E.F. Haney, M.J. Trimble, R.E.W. Hancock, Microtiter plate assays to assess antibiofilm activity against bacteria (2021), <https://doi.org/10.1038/s41596-021-00515-3>.
- [52] B.L. Furman, Streptozotocin-induced diabetic models in mice and rats, *Curr. Protoc.* 1 (4) (2021), <https://doi.org/10.1002/cpz1.78>.
- [53] I. Khalil, G. Quintens, T. Junkers, M. Dusselier, Muconic acid isomers as platform chemicals and monomers in the biobased economy, *Green. Chem.* 22 (5) (2020), <https://doi.org/10.1039/c9gc04161c>.
- [54] J. Ni, J. Di, C. Ma, Y.C. He, Valorisation of corncobs into furfuryl alcohol and furinic acid via chemoenzymatic cascade catalysis, *Bioresour. Bioprocess* 8 (1) (2021), <https://doi.org/10.1186/s40643-021-00466-3>.
- [55] M. Yavuz, et al., Temperature as a causative factor in diabetic foot ulcers: a call to revisit ulceration pathomechanics, *J. Am. Podiatr. Med. Assoc.* 109 (5) (2019), <https://doi.org/10.7547/17-131>.
- [56] T. Wang, et al., Smart composite hydrogels with pH-responsiveness and electrical conductivity for flexible sensors and logic gates, *Polymers (Basel)* 11 (10) (2019), <https://doi.org/10.3390/polym11101564>.
- [57] M.B. Dharmasiri, T.K. Mudiyanselage, Thermo-responsive poly(N-isopropyl acrylamide) hydrogel with increased response rate, *Polym. Bull.* 78 (6) (2021), <https://doi.org/10.1007/s00289-020-03270-9>.
- [58] P. Ferruti, J. Alongi, E. Barabani, A. Manfredi, E. Ranucci, Silk/polyamidoamine membranes for removing chromium VI from water, *Polymers (Basel)* 15 (8) (2023), <https://doi.org/10.3390/polym15081871>.
- [59] S. Shekhar, M. Mukherjee, A.K. Sen, Studies on thermal and swelling properties of Poly (NIPAM-co-2-HEA) based hydrogels, *Adv. Mater. Res.* 1 (4) (2012), <https://doi.org/10.12989/amr.2012.1.4.269>.
- [60] Q. Gao, C. Li, M. Wang, J. Zhu, C. Gao, A low-hysteresis, self-adhesive and conductive PAA/PEDOT:PSS hydrogel enabled body-conformable electronics', *J. Mater. Chem. C. Mater.* 11 (27) (2023) <https://doi.org/10.1039/d3tc00850a>.
- [61] J.B. da Silva, M.T. Cook, M.L. Bruschi, Thermoresponsive systems composed of poloxamer 407 and HPMC or NaCMC: mechanical, rheological and sol-gel transition analysis, *Carbohydr. Polym.* 240 (2020), <https://doi.org/10.1016/j.carbpol.2020.116268>.
- [62] M.M. Al-Rajabi, T.Y. Haan, Green synthesis of thermo-responsive hydrogel from oil palm empty fruit bunches cellulose for sustained drug delivery, *Polymers (Basel)* 13 (13) (2021), <https://doi.org/10.3390/polym13132153>.
- [63] M. Passamonti, C. de Roos, P.J. Schoenmakers, A.F.G. Gargano, Poly(acrylamide-co-N,N'-methylenebisacrylamide) monoliths for high-peak-capacity hydrophilic-interaction chromatography-high-resolution mass spectrometry of intact proteins at low trifluoroacetic acid content, *Anal. Chem.* 93 (48) (2021), <https://doi.org/10.1021/acs.analchem.1c03473>.
- [64] E. Sanchez Armengol, B. Grassiri, A.M. Piras, Y. Zambito, A. Fabiano, F. Laffleur, Ocular antibacterial chitosan-maleic acid hydrogels: in vitro and in vivo studies for a promising approach with enhanced mucoadhesion, *Int. J. Biol. Macromol.* 254 (2024), <https://doi.org/10.1016/j.ijbiomac.2023.127939>.
- [65] C.D. McArdle, K.M. Lagan, D.A. McDowell, Effects of pH on the antibiotic resistance of bacteria recovered from diabetic foot ulcer fluid: an in vitro study, *J. Am. Podiatr. Med. Assoc.* 108 (1) (2018), <https://doi.org/10.7547/16-033>.
- [66] C. McArdle, K. Lagan, S. Spence, D. McDowell, Diabetic foot ulcer wound fluid: the effects of pH on DFU bacteria and infection, *J. Foot Ankle Res.* 8 (2015), <https://doi.org/10.1186/1757-1146-8-s1-a8> no. S1.
- [67] Y. Wang, F. Miao, J. Bai, Z. Wang, W. Qin, An observational study of the pH value during the healing process of diabetic foot ulcer, *J. Tissue Viability* 33 (2) (2024) 208–214, <https://doi.org/10.1016/j.jtv.2024.03.015>.
- [68] X. Chen, et al., Evaluation of the bioactivity of a mastoparan peptide from wasp venom and of its analogues designed through targeted engineering, *Int. J. Biol. Sci.* 14 (6) (2018), <https://doi.org/10.7150/ijbs.23419>.
- [69] A.P. Kourtis, et al., Morbidity and mortality weekly report vital signs: epidemiology and recent trends in methicillin-resistant and in methicillin-susceptible *Staphylococcus aureus* bloodstream infections—United States, *Morb. Mortal. Wkly. Rep.* 68 (9) (2017).
- [70] S. Phan, et al., Relative Abundance and Detection of *Pseudomonas aeruginosa* from Chronic Wound Infections Globally (2023), <https://doi.org/10.3390/microorganisms11051210>.
- [71] X. Li, S. Zuo, B. Wang, K. Zhang, Y. Wang, Antimicrobial mechanisms and clinical application prospects of antimicrobial peptides, *Molecules* 27 (9) (2022), <https://doi.org/10.3390/molecules27092675>.
- [72] S.K. Zhang, et al., Design of an  $\alpha$ -helical antimicrobial peptide with improved cell-selective and potent anti-biofilm activity, *Sci. Rep.* 6 (2016), <https://doi.org/10.1038/srep27394>.
- [73] N. Jochumsen, et al., The evolution of antimicrobial peptide resistance in *Pseudomonas aeruginosa* is shaped by strong epistatic interactions, *Nat. Commun.* 7 (2016), <https://doi.org/10.1038/ncomms13002>.
- [74] W. Xia, et al., Poly(N-isopropylacrylamide-co-vinyl acetate)/poly(l-lactic acid) composite with thermoresponsive wettability, *Colloids Surf. A Physicochem Eng. Asp.* 636 (2022), <https://doi.org/10.1016/j.colsurfa.2021.128179>.
- [75] M.M. Rana, H.De La, Hoz Siegler, Tuning the properties of pnpam-based hydrogel scaffolds for cartilage tissue engineering, *Polymers (Basel)* 13 (18) (2021), <https://doi.org/10.3390/polym13183154>.
- [76] M.J. Ansari, et al., Poly(N-isopropylacrylamide)-Based Hydrogels for Biomedical Applications: A Review of the State-of-the-Art (2022), <https://doi.org/10.3390/gels8070454>.